

Gas transport in firn: multiple-tracer characterisation and model intercomparison for NEEM, Northern Greenland - Supplementary Material

C. Buizert¹, P. Martinerie², V. V. Petrenko³, J. P. Severinghaus⁴, C. M. Trudinger⁵, E. Witrant⁶, J. L. Rosen⁷, A. J. Orsi⁴, M. Rubino^{1,5}, D. M. Etheridge^{1,5}, L. P. Steele⁵, C. Hogan⁸, J. C. Laube⁸, W. T. Sturges⁸, V. A. Levchenko⁹, A. M. Smith⁹, I. Levin¹⁰, T. J. Conway¹¹, E. J. Dlugokencky¹¹, P. M. Lang¹¹, K. Kawamura¹², T. M. Jenk¹, J. W. C. White³, T. Sowers¹³, J. Schwander¹⁴, and T. Blunier¹

¹Centre for Ice and Climate, Niels Bohr Institute, University of Copenhagen, Juliane Maries vej 30, DK-2100 Copenhagen Ø, Denmark

²Laboratoire de Glaciologie et Géophysique de l'Environnement, CNRS, Université Joseph Fourier-Grenoble, BP 96, 38 402 Saint Martin d'Hères, France

³Institute of Arctic and Alpine Research, University of Colorado, Boulder, CO 80309, USA

⁴Scripps Institution of Oceanography, University of California, San Diego, La Jolla, CA 92093, USA

⁵Centre for Australian Weather and Climate Research/CSIRO Marine and Atmospheric Research, Aspendale, Victoria, Australia

⁶Grenoble Image Parole Signal Automatique, Université Joseph Fourier/CNRS, Grenoble, France

⁷Department of Geosciences, Oregon State University, Corvallis, OR 97331-5506, USA

⁸School of Environmental Sciences, University of East Anglia, Norwich, NR4 7TJ, UK

⁹Australian Nuclear Science and Technology Organisation, Locked Bag 2001, Kirrawee DC NSW 2232, Australia

¹⁰Institut für Umweltphysik, University of Heidelberg, INF 229, 69120 Heidelberg, Germany

¹¹NOAA Earth System Research Laboratory, Boulder, Colorado, USA.

¹²National Institute of Polar Research, 10-3 Midorichou, Tachikawa, Tokyo 190-8518, Japan

¹³The Earth and Environmental Systems Institute, Penn State University, 317B EESB Building, University Park, PA 16802, USA

¹⁴Climate and Environmental Physics, Physics Institute, University of Bern, Sidlerstrasse 5, CH-3012 Bern, Switzerland

1 Introduction

This document serves as a supplement to ‘*Gas transport in firn: multiple-tracer characterisation and model intercomparison for NEEM, Northern Greenland*’. It aims to provide more background information on the methods, as well as present additional modeling results which were omitted in the main article to improve readability. Most results from the US borehole are presented here. All firn air data and atmospheric reconstructions used in the study are included with this document.

The structure of this document closely follows that of the main text. Sections marked with a dagger (†) in the main article have a corresponding section here, where additional information can be found.

2 Methods

2.1 NEEM 2008 firn air campaign

The location of the North Greenland Eemian ice drilling project (NEEM) camp and the site of the 2008 firn air campaign are shown in Fig. 1. The firn air sampling location was selected according to the following criteria: (1) avoid contamination from the main camp (generator and vehicles) by going upwind of the most frequent wind direction (2) keep at least 1 km away from the skiway (3) keep a reasonable distance to the main camp in order to limit time for movement of cargo, ice cores and persons (4) keep outside the designated clean sector, a 90 degree sector between SE (along skyway) and SW.

A good compromise was found at 1.5 km SW (220°) from the main camp: 77.43° N, 51.10° W, at the edge of the NEEM clean sector (Fig 1). The main sampling was done from 2 holes (EU: S2 and US: S3) separated 63.5 meter. A 16 kW generator was placed at 80 m distance downwind. In order to minimise air contamination, vehicles were parked near the generator and within the last 80 m all equipment

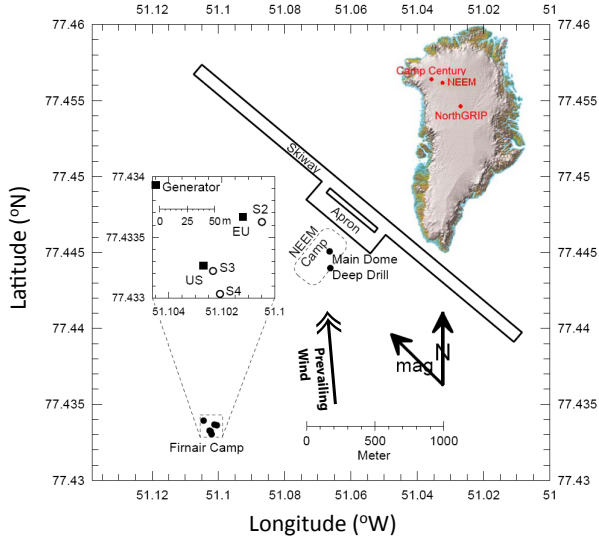


Fig. 1. Location of NEEM main structures and the site of the 2008 firn air campaign. The inset shows the position of the NEEM camp in Northern Greenland.

was transported by manhauling. Drilling was performed alternatively in both holes with the Danish electromechanical shallow drill. The hole diameter is 103.6 mm. In order to have an undisturbed surface for the first sampling levels, the first 10 m were drilled with a hand auger producing the same diameter core and hole.

The sampling depths of the two boreholes are listed in Table 1.

2.2 Physical characterisation of NEEM firn air site

For the density profile we use a fit to the NEEM main core density data averaged over 0.55m segments (Johnsen, personal communication, 2009). For the three stages of densification (Arnaud et al., 2000) we use a separate fit. Data fitting was done by eye, and care was taken that the second derivative is continuous over the transitions between the stages. Surface density was chosen as $\rho = 0.35 \text{ g cm}^{-3}$ (Heron and Langway, 1980). The densities between the surface and 16 m depth were fit with an equation of the form:

$$\rho = a_1 + a_2 z + a_3 e^{a_4(16-z)} \quad (1)$$

For the second stage $16 \leq z < 110 \text{ m}$ (or $0.55 < \rho < 0.85 \text{ g cm}^{-3}$) data were fit to a quadratic:

$$\rho = a_5 + a_6 z + a_7 z^2 \quad (2)$$

One data point, near 78 m, was rejected as an outlier. The rationale for using a quadratic instead of a more complex equation is that bubble closure parameterisations depend on the derivative of the density, and it is desirable that this

Table 1. Firn air sampling depths in meters for the EU (S2) and US (S3) boreholes.

Level	EU depth (m)	US depth (m)
0	0.00	0.00
1	2.50	2.85
2	4.90	5.23
3	7.55	9.83
4	10.10	19.30
5	14.80	34.70
6	19.75	49.70
7	27.54	57.47
8	34.72	59.90
9	42.42	62.00
10	50.00	64.03
11	54.90	65.50
12	57.40	66.90
13	59.90	68.30
14	61.95	69.80
15	63.85	71.40
16	65.75	72.85
17	68.05	73.80
18	70.05	75.60
19	72.00	-
20	74.08	-
21	75.90	-
22	77.75	-

derivative decreases monotonically in order to match inert gas observations of close-off fractionation processes (Severinghaus and Battle, 2006). For the third stage $z \geq 110 \text{ m}$ we use

$$\rho = a_8 + a_9 \left(1 - e^{a_{10}(z-110)}\right) \quad (3)$$

where again the constants a_8 , a_9 , and a_{10} are found by the requirement that the derivatives of the two curves match at 110 m, combined with the ice density (taken to be $\rho_{\text{ice}} = 0.9206 \text{ g cm}^{-3}$ at the temperature of -28°C). No data were used in this process, because the problem is already constrained (for three parameters with three constraints). The exponential was chosen to simulate the gradual compression of bubbles in the top 800 m of the ice sheet. The value of a_{10} found in this manner is approximately the inverse of 200 m, suggesting this value for a scale height. The critical value of 110 m was chosen primarily to yield this scale height (the scale height is strongly affected by the derivative of the quadratic at the critical point).

The primary subjective choices in this analysis were the choices of critical depths (16 and 110 m), the choice of fitting equations, and the choice of 0.35 g cm^{-3} as the surface density value (parameter a_1). The constants in Eqs. (1-3) obtained in the fitting procedure can be found in Table 2. The density data together with the fit are shown in Fig. 1 of the main document.

Table 2. Constants used in the density fitting Eqs. (1-3).

Constant		
a_1	3.500000	$\times 10^{-1}$
a_2	1.359319	$\times 10^{-2}$
a_3	-1.569421	$\times 10^{-2}$
a_4	-4.300000	$\times 10^{-1}$
a_5	4.332293	$\times 10^{-1}$
a_6	7.976252	$\times 10^{-3}$
a_7	-3.536121	$\times 10^{-5}$
a_8	8.82746379	$\times 10^{-1}$
a_9	3.7853621	$\times 10^{-2}$
a_{10}	-5.198599	$\times 10^{-3}$

The parameterisation of the open porosity to closed porosity ratio is described in Goujon et al. (2003). The closed porosity (s_{cl}), as a function of total porosity s and close-off porosity (s_{co}), is:

$$s_{cl} = 0.37s \left(\frac{s}{s_{co}} \right)^{-7.6} \quad (4)$$

Where the close-off porosity can be calculated from the “mean” close-off density ρ_{co} : $s_{co} = 1 - \rho_{co}/\rho_{ice}$. Equation 4 is consistent with the mean close-off density parameterisation by Martinerie et al. (1994) derived from total gas content measurements in ice cores. Changing s_{co} results in changing the complete close-off depth ($s_{op} = 0$). Field data indicate the last successful air pumping depth in firn and a depth at which no air could be extracted. The depth at which open firn porosity becomes zero should be located in this interval.

Using the mean close-off density of Martinerie et al. (1994) in the closed porosity equation (Eq. (4)) generally gives a complete close-off depth ($s_{op} = 0$) inconsistent with field data. The cause of this discrepancy is not clear; it could be due to e.g. firn heterogeneity, or biases and uncertainties in firn density measurements. In the case of NEEM, it leads to a complete close-off depth higher than the last measurement depth. This discrepancy may be due (for example) to the effect of heterogeneities in firn on the complete close-off depth. A different mean close-off density value is used in order to obtain a complete close-off depth consistent with field data. In the case of NEEM, the last successful air pumping depth was $z = 77.75$ m, and a decreased air flow rate (which did not allow for sampling) was observed at $z = 79$ m depth. It was thus considered that air was isolated from the atmosphere at that depth, and used 78.8 m as the zero open porosity level (this is equivalent to a mean close-off density of $\rho_{co} = 0.8312$ gcm⁻³ in Eq. (4)).

The accumulation rate estimate is based on the dated NEEM 2007 shallow S1 core (Dahl-Jensen, personal communication, 2010). The derived variations of the accumulation rate with time are shown in Fig. 2. For all the tracers we run the models from 1800 to the sampling date 2008.54. As a

Table 3. Overview of laboratories that supplied firn air data. Included are the School of Environmental Sciences at the University of East Anglia (UEA), NOAA Earth System Research Laboratory, Boulder CO (NOAA), the Institut für Umweltphysik at the University of Heidelberg (IUP), the Commonwealth Scientific and Industrial Research Organisation, Marine and Atmospheric Research (CSIRO), the Australian Nuclear Science and Technology Organisation (ANSTO), National Institute of Polar Research, Japan (NIPR), and Scripps Institution of Oceanography at the University of California, San Diego (SIO).

Tracer	EU borehole	US borehole
CO ₂	NOAA, CSIRO, IUP	NOAA, IUP
CH ₄	NOAA, CSIRO	NOAA, IUP
SF ₆	NOAA, IUP, UEA	NOAA, IUP
CFC-11	UEA	-
CFC-12	UEA	-
CFC-113	UEA	-
HFC-134a	UEA	-
CH ₃ CCl ₃	UEA	-
$\Delta^{14}\text{CO}_2$	ANSTO	-
$\delta^{15}\text{N}_2$	NIPR/SIO	NIPR/SIO
$\delta^{86}\text{Kr}^*$	NIPR/SIO	NIPR/SIO

* Used for gravitational correction only.

best estimate of the accumulation rate we use the mean value over this period of $A = 0.216$ myr⁻¹ ice equivalent. The best estimate for the current day value is $A = 0.227$ myr⁻¹, which is within the range of variability observed in the past.

2.3 Gas measurements

The firn air measurements used in this study are listed in Table 3.

For SF₆, the IUP data (EU and US holes) have been rescaled by 0.9912 to place the data on the NOAA scale that we use in our atmospheric reconstructions (rescaling corresponds to a modern day offset of 0.06 ppt). The NOAA and UEA SF₆ data were provided on the NOAA scale. After correcting the IUP data no inter-laboratory offsets were observed on either borehole.

For the US hole NOAA CH₄ data have been used exclusively where available (13 depth levels). For a remaining 5 depths we have no NOAA measurements, and for these depths we have used IUP data after scaling them in the following way to place them on the NOAA scale:

$$[\text{CH}_4]_{\text{NOAA}} = 0.9933[\text{CH}_4]_{\text{IUP}} + 10.12 \quad (5)$$

This equation was obtained by correlating NOAA and IUP data on the US hole for depths where we have data from both labs (13 depths, $R^2 = 0.9995$). The NOAA and CSIRO data on the EU borehole agree well and show no systematic offset.

Table 4 lists the radiocarbon measurements. CO₂ was extracted in May 2009 from 0.5 L glass sample flasks also

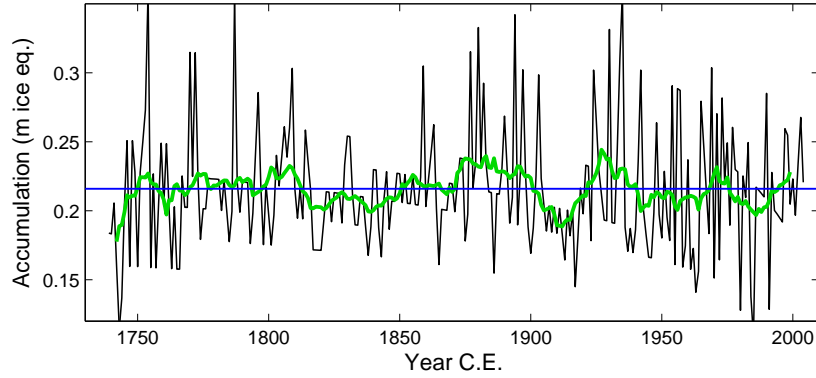


Fig. 2. Accumulation rate estimate from the NEEM 2007 S1 shallow core. The black line shows the yearly values, the green line gives a running 15 year average and the blue horizontal line shows the average value over the modeled period 1800-2008.

Table 4. Overview of radiocarbon measurements on NEEM firn air, expressed in $\Delta^{14}\text{C}$ notation. The replicate dev. gives the deviation of the replicate measurement from the first one.

Depth (m)	$\Delta^{14}\text{C}$ (‰)	ANSTO error (‰)	Replicate dev. (‰)	Flask type
0.00	44.9	6.3	-	Glass
14.80	40.1	6.8	-	Glass
34.72	55.9	6.2	-	Glass
50.00	64.9	6.8	-	Glass
59.90	74.5	6.9	-	Glass
61.95	76.3	6.8	-	Glass
65.75	156.0	7.5	5.9	Glass
68.05	276.1	7.6	3.4	Glass, Stainless
70.05	349.0	6.3	-	Stainless
72.00	309.3	8.2	0.5	Glass, Stainless
74.08	165.4	7.3	-	Glass
75.90	45.1	7.2	4.8	Glass

used for CSIRO gas analysis, and in September 2009 the extracted CO_2 was graphitised at ANSTO. Measurements of $\Delta^{14}\text{CO}_2$ were performed on the ANTARES accelerator mass spectrometer (Fink et al., 2004). Since the sample collected at 70.05 m depth was lost during the initial graphitisation, it was extracted again in October 2009 from air samples collected in 3 L stainless steel containers also used for CSIRO gas analysis, and measured in January 2010. The samples collected at 68.05 and 72 m depth were extracted together with the lost 70 m sample, to check for any discrepancy between the first (May 2009) and the second (October 2009) extraction. The replicates agreed within the estimated uncertainty of the graphitisation at ANSTO. Since the samples were measured shortly after sampling, there is no need to correct for the decay that occurred within the flasks.

From these $\Delta^{14}\text{C}$ values we convert to a mass conserving mole fraction $^{14}\text{CO}_2$ using

$$^{14}\text{CO}_2 = \left(\frac{\Delta^{14}\text{C}}{1000} + 1 \right) \left(\frac{\delta^{13}\text{C}/1000 + 1}{-25/1000 + 1} \right)^2 \times A_{\text{abs}} \times [\text{CO}_2] \quad (6)$$

where we use the commonly used value of $A_{\text{abs}} = 1.1764 \times 10^{-12}$ (Karlen et al., 1968). The values of $\delta^{13}\text{C}$ and $[\text{CO}_2]$ are known from measurements of NEEM firn air from CSIRO Aspendale. Note that in the $\Delta^{14}\text{C}$ notation used here the activity of the isotopic reference material is decay-corrected, whereas the activity of the sample is not. Decay correction of the sample is not necessary, and simply not possible since the firn samples have an unknown mixture of ages. Sample decay is included through a decay term in the firn air models (Trudinger et al., 1997).

The $\delta^{15}\text{N}_2$ data used as a tracer is corrected for the effect of thermal fractionation following the method described in Severinghaus et al. (2001). In this method the observed

$\delta^{15}\text{N}_{\text{obs}}$ is split up as $\delta^{15}\text{N}_{\text{obs}} = \delta^{15}\text{N}_{\text{grav}} + \delta^{15}\text{N}_{\text{therm}}$, where the right hand side consists of a gravitational and a thermal term respectively. The gravitational fractionation scales linearly with the mass difference ΔM between the isotopologues. The thermal diffusion term $\delta^{15}\text{N}_{\text{therm}}$ is calculated using borehole temperature measurements and the SIO firn air model. This way one can solve for $\delta^{15}\text{N}_{\text{grav}}$.

2.4 Reconstruction of atmospheric histories of selected tracers

2.4.1 Combining different data series

The first major issue for combining different data series is calibration scale, which is not always fully documented in available metadata. In the case of AGAGE, all available data (ALE, GAGE and AGAGE) are on the same scale (SIO-2005). NOAA halocarbon data are currently under re-analysis. For this study only data converted to the most recent calibration scale were used (Geoff Dutton and Bradley Hall, personal communication).

Calibration (and/or procedural) differences between different atmospheric networks are less documented and understood. Synthetic results of intercomparisons between AGAGE and NOAA halocarbon data were kindly provided to the NEEM gas group (Paul Krummel, personal communication); they are shown in Table 5. Two different comparison results are provided: comparisons of atmospheric data at a common measurement site (American Samoa) and comparisons of air tanks circulated around measurement labs (IHALACE: International HALocarbons in Air Comparison Experiment; Bradley Hall, personal communication). The comparisons are consistent for CFC-12 and CFC-113. Concentration ratios at American Samoa are time-dependent for CFC-11. For CH_3CCl_3 Samoa and IHALACE results are inconsistent (note that IHALACE tanks had low concentration levels), and different results are obtained with Electron Capture Detector (ECD) and Gas chromatography-mass spectrometry (GCMS). As old trend data were obtained with ECD, GCMS measurements are not used for this species; a NOAA/AGAGE ratio of 1.035 is used.

2.4.2 Description of the reconstructions

CO₂: Summit and Alert NOAA-ESRL monthly record from 6/1985 - 12/2008. For months when both Summit and Alert records are available we use the average of the two. For months when only data from either one of the stations is available that station is used, with a correction for the average Alert-Summit offset for that given month. Mauna Loa (MLO) NOAA-ESRL (7/1976-5/1985) and SIO (3/1958-6/1976) records are used for indicated periods with a latitudinal correction applied based on the mean of the modern day MLO-Summit and MLO-Alert offset. Plots for offset

vs. time revealed no trend, so a constant correction is used. A months 2-4/1964 gap in the SIO MLO record is filled by linear interpolation.

Prior to the MLO instrumental record, mean annual values are based on the the Law Dome mean-annual 20-yr smoothed record (1832-1958) and the Law Dome 75-yr smoothed mean annual record (1800-1831) (Etheridge et al., 1996), corrected for the Law Dome-NEEM offset. For missing years data points are interpolated linearly. Both the value and the trend of the Law Dome-NEEM offset were determined for the period 1959-1978 where the records overlap. In 1931 this results in NEEM concentration equaling the Law Dome concentration, so the inter-polar gradient goes to zero. For simplicity, beyond this point we simply set NEEM equal to Law Dome. A seasonal CO₂ cycle is added based on NEEM reconstructed monthly values for 1959-2008.

CH₄: Summit and Alert NOAA-ESRL monthly record from 6/1985-12/2008. For months when the Summit record is available, NEEM is set equal to Summit. For months where Summit record is unavailable, the NEEM reconstruction is based on Alert with a correction for the Summit-Alert offset for that month applied. Alert-Summit offsets show no significant trends with time.

Prior to the Alert record mean annual values are based on the Law Dome firn record (1978-1985) and the Law Dome ice core record (1800-1978) (Etheridge et al., 1998), scaled by 1.0124 to convert the data to the NOAA 2004 CH₄ calibration scale, and with a correction applied for the Law Dome-NEEM offset. The inter-polar gradient (IPG) is assumed to be constant at 45 ppb from 1800-1885 (Etheridge et al., 1998). For 1886-1985 it is assumed that the IPG is a function of both Law Dome [CH₄] and $d[\text{CH}_4]/dt$. The IPG correction is tuned to the period 1986-1998 where direct atmospheric measurements are available and there is an appreciable growth rate $d[\text{CH}_4]/dt$. A seasonal CH₄ cycle is added based on the reconstructed NEEM monthly values for 1986-2008. It is assumed that the amplitude of the seasonal cycle is directly proportional to the mean annual concentration.

¹⁴CO₂: The atmospheric ¹⁴CO₂ record from Fruholmen, Norway, is used for its proximity to Greenland, from 1/1963-6/1993 (Nydal and Lövseth, 1996). Atmospheric measurements from central Europe have been used from 6/1993-12/2008 (Vermunt and Jungfraujoch, Levin et al., 2008) and from 2/1959-12/1962 (Vermunt, Levin and Kromer, 2004). In the period 1990-2010 the reconstruction agrees within a few per mil with a recent atmospheric record from Alert station (Levin et al., 2010), which was not yet available at the time we finalised the reconstruction.

Southern hemisphere atmospheric ¹⁴CO₂ measurements are used from 1954-1959 (Manning and Melhuish, 1994) with a correction of 30 ‰ on average to account for the interhemispheric gradient.

Table 5. Concentration ratios (NOAA/AGAGE) for halocarbon species.

Species	Multiple sites ^{a,b} flask/in-situ	Samoa ^a in-situ/in-situ	IHALACE ^c	This study (prelim.IHALACE)	Scales	Comment
CFC-11	1.0100	1.0095	1.0058	1.0081	NOAA-1993/SIO-05	time dependent
CFC-11	1.0057	1.0080	-	1.0081	NOAA-1993/SIO-05	2007-2009 only
CFC-12	0.9973	0.9965	0.9978	0.9978	NOAA-2008/SIO-05	
CFC-113	1.0199	1.0251	1.0266	1.0215	NOAA-2003/SIO-05	
CH ₃ CCl ₃	1.0339	1.0379	1.0572 / - ^d	1.0627 / 1.0526 ^d	NOAA-2003/SIO-05	ECD detector
CH ₃ CCl ₃	1.0158	-	1.0081 / - ^d	1.0081 / 1.0030 ^d	NOAA-2003/SIO-05	GCMS detector

^a Krummel, personal communication

^b Based on Mace Head, Trinidad Head, Samoa and Cape Grim

^c Hall, B.D., Engle, A., Mühle, J., Elkins, J. et al., Results from the International Halocarbons in Air Comparison Experiment (IHALACE), in preparation

^d Ratios for tanks at 22 ppt and 18 ppt respectively

Prior to 1955 no direct atmospheric records exist and the reconstruction is equal to $\Delta^{14}\text{CO}_2$ reconstructed from dendrochronologically dated tree-ring samples (Reimer et al., 2004). The atmospheric $\Delta^{14}\text{CO}_2$ has been converted to a ppm scale using Eq. (6).

It should be noted that, unlike the firn air ^{14}C measurements, the atmospheric histories have been age-corrected for decay between the time that the sample was “collected” (in the case of trees, since the tree removed the CO_2 from the air), and the time that the sample was measured.

$\delta^{13}\text{CO}_2$: A $\delta^{13}\text{CO}_2$ reconstruction is required to convert $\Delta^{14}\text{CO}_2$ values from a permil scale to a mass-conserving ppm scale as described by Eq. (6). The Alert CSIRO monthly record from 1/1990-6/2008 is used without correction.

Prior to the Alert record we use the Cape Grim air archive record (1978-1989) and the Law Dome ice core record (1800-1978) (Francey et al., 1999), with a correction applied for the Law Dome-NEEM offset. The correction is assumed to scale linearly with the atmospheric growth rate of CO_2 , and is calibrated to the period 1990-2008 where CSIRO Alert and Cape Grim monthly records are available.

CFC-11: Emission-based model results from Martinerie et al. (2009) before 7/1978. Mid Northern latitudes combined AGAGE monthly record 7/1978-3/2009. Overall scenario converted to NOAA scale with NOAA/AGAGE=1.0081 (IHALACE).

CFC-12: Mid Northern latitudes combined AGAGE monthly record 1/1981- 3/2009 (early record ignored because of missing data and high inter-hemispheric gradient). 2D model results from Martinerie et al. (2009) before. Overall scenario converted to NOAA scale with NOAA/AGAGE=0.9978 (IHALACE).

CFC-113: Mid Northern latitudes combined AGAGE monthly record 6/1986- 3/2009 (early record ignored because of missing data and high inter-hemispheric gradient).

Emission-based model results from Martinerie et al. (2009) before. Overall scenario converted to NOAA scale with NOAA/AGAGE=1.0215 (IHALACE).

SF₆: Barrow NOAA-ESRL combined (Geoff Dutton) monthly record 1/1999- 7/2009 (Barrow data for 1995-1998 ignored because of variable N/S gradient. Emission-based model results from Martinerie et al. (2009) before.

CH₃CCl₃: Mid Northern latitudes combined AGAGE monthly record 7/1978- 3/2009. Emission-based model results before 7/1978 (visual rescaling by 1.05). Overall scenario converted to NOAA scale with a NOAA/AGAGE ratio of 1.035 (Samoa data with ECD detection).

HFC-134a: Barrow NOAA monthly record 2/1995- 3/2009, Emission-based model results before 02/1995 (visual rescaling by 1.10).

The mid-latitude AGAGE data could not be extrapolated to high latitudes for halocarbons. The first reason is the highly time dependent meridional concentration gradients; for species phased out under the Montreal Protocol, due to strongly reduced emissions, even the inter-polar gradient is close to zero in recent years. Another difficulty arises from the fact that the NOAA-ESRL mid Northern latitude site (Niwt Ridge) is a high altitude site, thus the effects of altitude and latitude on concentrations cannot be separated.

$\delta^{15}\text{N-N}_2$: There is no need for a $\delta^{15}\text{N-N}_2$ reconstruction since the isotopic composition of Nitrogen is constant in the atmosphere on the timescales considered here. Formally, calculating the isotopic ratio would require both $^{15}\text{N}^{14}\text{N}$ and $^{14}\text{N}^{14}\text{N}$ isotopologues to be modeled separately. However, the $^{14}\text{N}^{14}\text{N}$ isotopologue constitutes nearly 80% of the air molecules, violating the assumption used by the firn models of modeling diffusion of trace gases into air. We have instead chosen to use an atmospheric forcing $[^{15}\text{N}^{14}\text{N}](t) = 1$ for all t , and we assume that the $^{14}\text{N}^{14}\text{N}$ isotopologue has

unity mixing ratio everywhere $[^{14}\text{N}^{14}\text{N}](z) = 1$. This is tantamount to assuming that $^{14}\text{N}^{14}\text{N}$ is the only non-trace gas in air (molecular diffusivity of $^{15}\text{N}^{14}\text{N}$ into air is used, however, rather than $^{15}\text{N}^{14}\text{N}$ into $^{14}\text{N}^{14}\text{N}$). The $\delta^{15}\text{N-N}_2$ signal is then given as $\delta^{15}\text{N-N}_2(z) = 10^3 \times ([^{15}\text{N}^{14}\text{N}](z) - 1)$.

2.4.3 Uncertainty estimates on atmospheric reconstructions

Table 6 summarises the elements used for the uncertainty estimates. The dates refer to the period for which the comparison was made (thus the uncertainty should be applied from the beginning of the earliest data series to the end date of the comparison). The biases between labs can be large and time varying for halocarbons. To distinguish the mean bias from the variability of the differences between data series, these variabilities are noted dev. instead of σ , because the distributions are obviously not Gaussian in many cases.

Uncertainties are overall much higher for halocarbons than for other gases. For halocarbons, uncertainties on emissions are likely more pessimistic than uncertainties on concentrations. As an illustration, Martinerie et al. (2009) rescaled halocarbon emissions so that modeled atmospheric concentrations fit the early part of atmospheric datasets. Rescaling factors for CFC-11, CFC-12, CFC-113, CCl_4 and SF_6 range between 5 and 10% for the rising part of the trends.

Niwort Ridge halocarbon concentrations are mostly lower than Barrow concentrations, suggesting a dominant effect of altitude rather than latitude. Differences between Summit and Barrow are much lower. This suggests that the mid-latitude to Greenland concentration gradient is within the noise on the data for halocarbons.

Using the values in Table 6 uncertainties are constructed in the following way:

CO₂ uncertainties: 1985-2008: half the ALT/SUM offset, 1976-1985: half the ALT/SUM offset and the standard deviation of the ALT/MLO-NOAA offset, 1958-1976: half the ALT/SUM offset and the standard deviation of the ALT/MLO-SIO offset, 1930-1958: twice the 1σ Law Dome measurement uncertainty, the IPG uncertainty estimate, 1800-1930: three times the 1σ Law Dome uncertainty and the IPG uncertainty estimate. In each period the listed terms are added quadratically to estimate the total uncertainty.

CH₄ uncertainties: The CH₄ uncertainty is dominated by the uncertainty in the IPG estimate, which is large for CH₄. For this reason three independent reconstructions were made, and the uncertainty was taken as the maximum difference between the reconstructions. The first method is described in Sect. 2.4.2, a second method assumes the IPG is linearly related to the CH₄ mixing ratio, a third method uses the a linear regression analysis between atmospheric

growth rate and IPG. The comparison leads to an uncertainty ranging from 5-42 ppb.

For halocarbons, expressing emission-related uncertainties in % results in an unrealistic zero uncertainty at the start date of emissions. Thus somewhat arbitrarily, a minimum absolute uncertainty (in ppt) was set to the present-day uncertainty. The large increase in uncertainty when switching from atmospheric records to emission based estimates is applied gradually (over about 2 years) for all halocarbon species.

CFC-11 uncertainties: 1995-2010: 1.5%, 1990-1994: 2.5%, 1978-1989: 3.5%, before 1978: 18%. The changes in uncertainty after 1978 roughly reflect an increasing bias between AGAGE and NOAA measurements when going back in time.

CFC-12 uncertainties: 1996-2010: 0.5%, 1981-1995: 2%, before 1981: 7.5%.

CFC-113 uncertainties: 1996-2010: 1%, 1986-1995: 2.5%, before 1986: 8.4%.

SF₆ uncertainties: 1999-2010: 1.5%, 1985-1998: 3.5% South. Hem. and 5% North. Hem., 1978-1984: 3.5% South. Hem. and 10% North. Hem., before 1978: 40%. The high uncertainty on emissions reflects mismatches between bottom-up and top-down estimates (WMO, 2007). Levin et al. (2010) mention a 20% mismatch between their recent estimates.

CH₃CCl₃ uncertainties: 2000-2010: 4%, before 2000: 6%. These uncertainties are high compared to the 4.2% uncertainty on emissions from WMO (2007). They reflect the variability of the AGAGE/NOAA ratio and the dispersion around monthly mean values.

HFC-134a uncertainties: 2000-2010: 3%, 1995-1999: 6% before 1995: 8.4%.

$\Delta^{14}\text{CO}_2$ uncertainties: direct atmospheric records are long compared to other tracers, and the largest source of uncertainty is latitudinal gradients. Hua and Barbetti (2004) estimate that for the period 1955-1969 the maximum variability found between stations in the high latitude northern hemisphere is 18 ‰. This uncertainty exceeds the typical measurement precision of around 5 ‰ (Levin and Kromer, 2004). We therefore use the 18 ‰ estimate for our atmospheric reconstruction.

2.5 Gravitational correction

Before the modeling all data were corrected for the effect of gravity. The correction is made using the formula

Table 6. Elements for uncertainty estimates. ALT: Alert, Canada, BRW: Pt. Barrow, Alaska USA, MLO: Mauna Loa, Hawaii USA, SUM: Summit Greenland, ADR: Adrigole, Ireland, MHD: Mace Head, Ireland, CMO: Cape Meares, USA, THD: Trinidad Head, USA, CGO: Cape Grim, Tasmania, SPO: South Pole, Antarctica, Measurement types: cn (continuous), fl (flasks). Other notations: instrument names/types.

Species	Source	scale	dates	error	comment
CO ₂	Etheridge 1996	CSIRO	before 1942	1.1ppm	1 σ ice core data
	Etheridge 1996	CSIRO	1942-1958	0.1ppm	1 σ firn air data
	Inter-polar gradient	NOAA	before 1985	2ppm	Estimated IPG uncertainty
	NOAA website	NOAA	1997-2008	0.5ppm	mean bias (ALT/SUM)
	NOAA website	NOAA	1985-2008	0.8ppm	dev. of bias (ALT/MLO-NOAA)
	NOAA & GAW	-	1985-2008	0.8ppm	dev. of bias (ALT/MLO-SIO)
CH ₄	NOAA website	NOAA	2000-2008	0.15/2ppm	1 σ on monthly values (South/North)
	Etheridge 1998	CSIRO	before 1944	5 ppb	1 σ ice core data
	Etheridge 1998	CSIRO	1944-1978	2.2 ppb	1 σ firn air data
	Inter-polar gradient	NOAA	before 1985	5-42ppb	Difference between 3 IPG estimates
CFC-11	NOAA & GAW	NOAA	2000-2008	3/15ppb	1 σ on monthly values (South/North)
	WMO (2007)	emissions	before 1978	18%	Table 1-7, p1.44 in WMO (2007)
	AGAGE website	AGAGE	1980-1983	-0.2%	mean bias (ADR/THD)
	AGAGE website	AGAGE	1987-1989	-0.3%	mean bias (CMO/THD)
	AGAGE website	AGAGE	1996-2009	-0.07%	mean bias (MHD/THD)
	AGAGE & NOAA	-	1991-2009	-0.3%	mean bias (AGAGE/NOAA)
	AGAGE & NOAA	-	1991-2009	-1.1%	center/dev of bias (AGAGE/NOAA)
	AGAGE website	AGAGE	1995-2009	0.2/0.3ppt	1 σ on monthly values (South/North)
CFC-12	AGAGE website	AGAGE	1978-1995	1./1.5ppt	1 σ on monthly values (South/North)
	WMO (2007)	emissions	before 1981	7.5%	Table 1-7, p1.44 in WMO (2007)
	AGAGE website	AGAGE	1981-1983	+2.0%	mean bias (ADR/THD)
	AGAGE website	AGAGE	1987-1989	+0.4%	mean bias (CMO/THD)
	AGAGE website	AGAGE	1996-2009	-0.1%	mean bias (MHD/THD)
	AGAGE & NOAA	-	1991-2009	+0.3%	mean bias (AGAGE/NOAA)
	AGAGE & NOAA	-	after 1996	+0.1./1%	center/dev of bias (AGAGE/NOAA)
	AGAGE & NOAA	-	before 1996	+1.0/1.%	center/dev of bias (AGAGE/NOAA)
	AGAGE website	AGAGE	after 1996	.5/6ppt	1 σ on monthly values (South/North)
	AGAGE website	AGAGE	before 1996	1.5/3.ppt	1 σ on monthly values (South/North)
CFC-113	WMO (2007)	emissions	before 1986	8.4%	Table 1-7, p1.44 in WMO (2007)
	AGAGE website	AGAGE	1987-1989	-0.9%	mean bias (CMO/THD)
	AGAGE website	AGAGE	1996-2006	-0.2%	mean bias (MHD/THD md)
	AGAGE website	AGAGE	2005-2009	+0.01%	mean bias (MHD/THD medusa)
	AGAGE & NOAA	-	1996-2003	+0.04%	mean bias (AGAGE/NOAA)
	AGAGE & NOAA	-	1996-2003	+0.2/1%	center/dev of bias (AGAGE/NOAA)
	AGAGE website	AGAGE	after 1996	0.2/0.2ppt	1 σ on monthly values (South/North)
	AGAGE website	AGAGE	before 1996	0.6/1.0ppt	1 σ on monthly values (South/North)
SF ₆	WMO (2007)	emissions	before 1999	40.%	p1.51 in WMO (2007)
	NOAA website	NOAA	1998-2003	+0.2%	mean bias (cn/fl)
	AGAGE & NOAA	-	2001-2009	-0.9%	mean bias (AGAGE/NOAA)
	AGAGE & NOAA	-	2001-2009	-1./1.%	center/dev of bias (AGAGE/NOAA)
	NOAA website	NOAA	1997-2009	.06/0.05ppt	1 σ on monthly values (South/North)
CH ₃ CCl ₃	WMO (2007)	emissions	before 1978	4.2%	p1.45 in WMO (2007)
	AGAGE website	AGAGE	1981-1983	+3.5%	mean bias (ADR/THD)
	AGAGE website	AGAGE	1987-1989	+0.8%	mean bias (CMO/THD)
	AGAGE website	AGAGE	1996-2009	+0.09%	mean bias (MHD/THD)
	AGAGE website	AGAGE	2005-2009	+0.4%	mean bias (MHD/THD medusa)
	AGAGE & NOAA	-	1991-2009	+1.1%	mean bias (AGAGE/NOAA)
	AGAGE & NOAA	-	1991-2009	+1/4%	center/dev of bias (AGAGE/NOAA)
	AGAGE website	AGAGE	after 2000	0.3/0.4ppt	1 σ on monthly values (South/North)
	AGAGE website	AGAGE	before 2000	0.8/2.5ppt	1 σ on monthly values (South/North)
HFC-134a	WMO (2007)	emissions	before 1995	8.4%	Table 1-7, p1.44 in WMO (2007)
	NOAA website	NOAA	1995-2009	+0.1%	mean ALT/BRW
	AGAGE & NOAA	-	1998-2009	\pm 0.5%	mean bias (AGAGE/NOAA)
	AGAGE & NOAA	-	after 2000	+1/2.%	center/dev of bias (AGAGE/NOAA)
	AGAGE & NOAA	-	before 2000	+0/6.%	center/dev of bias (AGAGE/NOAA)
	NOAA website	NOAA	1995-2009	0.2/0.3ppt	1 σ on monthly values (South/North)
$\Delta^{14}\text{CO}_2$	(Hua and Barbetti, 2004)	-	1955-1969	18 ‰	latitudinal $\Delta^{14}\text{CO}_2$ variations

$$[\text{X}]_{\text{gravcorr}}(z) = \frac{[\text{X}]_{\text{meas}}(z)}{\Delta M(\delta_{\text{grav}}(z)/1000 + 1)} \quad (7)$$

where $[\text{X}]_{\text{gravcorr}}$ is the mixing ratio of gas species X after gravitational correction, $[\text{X}]_{\text{meas}}$ the mixing ratio as measured, $\Delta M = M_{\text{X}} - M_{\text{air}}$ is the difference in molar mass between gas X and air and $\delta_{\text{grav}}(z)$ is the gravitational fractionation per unit mass difference at depth z . The values of

$\delta_{\text{grav}}(z)$ are listed in Tables 7 and 8 for the EU and US boreholes, respectively. They are based on measurements of the gravitational enrichment of $\delta^{86}\text{Kr}$ ($^{86}\text{Kr}/^{82}\text{Kr}$) with depth, and corrected for the effect of thermal fractionation (Severinghaus et al., 2001). The rationale for using Kr rather than N_2 , is that its free-air diffusivity is closer to that of most of the tracers we use, so it should represent the disequilibrium effects on gravitational fractionation more accurately.

Table 7. Gravitational correction δ_{grav} for the EU hole.

Depth (m)	δ_{grav} (‰)
0.00	0.000
2.50	0.004
4.90	0.014
7.55	0.025
10.10	0.036
14.80	0.058
19.75	0.080
27.54	0.116
34.72	0.152
42.42	0.190
50.00	0.227
54.90	0.250
57.40	0.262
59.90	0.273
61.95	0.282
63.85	0.285
65.75	0.285
68.05	0.285
70.05	0.285
72.00	0.285
74.08	0.285
75.90	0.285
77.75	0.285

Table 8. Gravitational correction δ_{grav} for the US hole.

Depth (m)	δ_{grav} (‰)
0.00	0.000
2.85	0.005
5.23	0.015
9.83	0.035
19.30	0.078
34.70	0.152
49.70	0.226
57.47	0.262
59.90	0.273
62.00	0.282
64.03	0.285
65.50	0.285
66.90	0.285
68.30	0.285
69.80	0.285
71.40	0.285
72.85	0.285
73.80	0.285
75.60	0.285

2.7 Overall uncertainty estimation

When tuning to multiple gases it is important to have realistic uncertainty estimates for both the data and the atmospheric reconstruction. These will determine how much weight is given to the different gases during the tuning pro-

cedure. Therefore consistency between the different gases is more important than the absolute accuracy of the uncertainty estimates. Since the fit we obtain to the data is better than a 1σ Gaussian distribution, the assigned uncertainties are probably conservative. These uncertainties are not a fixed number for each gas, but can be expressed as a function of depth. The uncertainty estimate is based on seven potential sources of uncertainty, which are listed in the main text. Here we will discuss each in more detail.

2.7.1 Analytical precision

We use the analytical precision as specified by the laboratories that supplied the data. In case we have data from several laboratories for a single gas species, the largest of the specified uncertainties is used. Where there are multiple data points available for the same depth we additionally calculated the standard deviation between the data points. The assigned analytical uncertainty for a specific depth is taken as the larger of (1) the 1σ standard deviation for that depth and (2) the (depth independent) lab specified uncertainty.

2.7.2 Uncertainty in atmospheric reconstruction

The uncertainties in the atmospheric reconstructions, as described in Sect. 2.4.3, are produced on a time scale. By calculating the mean age of the gases, the estimates can be mapped from a timescale onto a depth scale. This is more practical from a modeling point of view. The conversion is done by treating the uncertainty estimate as a regular gas history, and running it through the CIC firn air model. This approach is valid since the diffusion model is linear with respect to the atmospheric input.

However, the complication that arises is the following: The depth estimates are used as *input* to the tuning procedure, but at the same time they rely on model *output* (the mean ages are calculated using the firn model). This could lead to a circular/iterative procedure where we refine the uncertainties indefinitely. To avoid this situation we use only the CIC model with near-finalised tuning, where the calculated mean ages are estimated to be off by only a few years. Since the uncertainty estimates do not have a temporal resolution better than a few years, we believe this approach to be valid. Furthermore, we have checked the validity of this approach afterwards, by re-calculating the mean ages after finalising the tuning of the model. Indeed the mean ages obtained by the nearly-finalised and finalised model tuning did not differ by more than four years in the deepest firn.

2.7.3 Sample contamination

For the deepest samples it becomes increasingly difficult to pump air from the firn. The reduced sample flow can lead to contamination due to incomplete flushing of flasks, and air leaking past the sealing bladder. Several halocarbon species should be absent at the deepest sampling levels, and we use

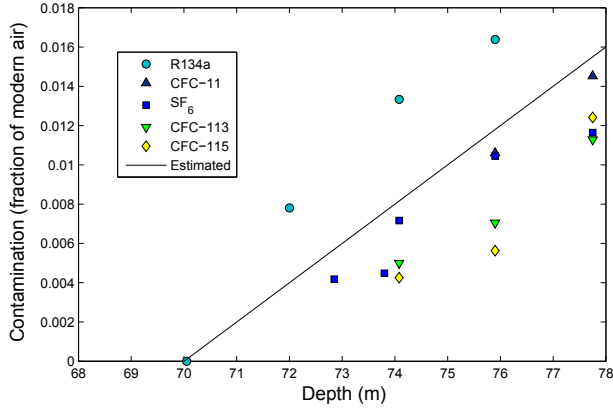


Fig. 3. Contamination as calculated from gas measurements, with in black the values used as the uncertainty estimate for contamination in all NEEM samples.

these to estimate sample contamination. All contaminations are assumed to be with modern air, and expressed as a fraction of sample volume.

Figure 3 shows estimates of sample contamination from different gases, and the contamination estimate for NEEM as the black line (1.6% contamination for the deepest samples). Note that we do not make any corrections to the data, but rather assign an additional uncertainty to the deepest samples because we have indication of contamination. The fraction of contaminated air is taken to be

$$\frac{V_{\text{contam}}}{V} = \begin{cases} 0 & \text{if } z < 70\text{m} \\ 0.016 \times (z - 70)/8 & \text{if } z \geq 70\text{m} \end{cases} \quad (8)$$

where V_{contam}/V is the fraction of the sample volume that comes from the modern atmosphere rather than from the open pores of the firn layer being sampled. The uncertainty introduced by the contamination is calculated by multiplying the fraction of modern air by the difference between modern atmospheric and measured firn air mixing ratios.

2.7.4 Sampling errors

The sampling procedure introduces errors which are not easily estimated. For CO_2 , CH_4 and SF_6 we have data from several labs, as well as from both boreholes. We use these to estimate the influence of the sampling procedure. IUP CH_4 and SF_6 data have been corrected as described in Sect. 2.3.

We treat each gas species and borehole separately. First, we consider sampling depths for which we have data from at least two labs, and calculate the standard deviation of the data for that depth. The sampling uncertainty is estimated as the average of the obtained standard deviations. The assigned sampling uncertainty for a specific depth is taken as the larger of (1) the 1σ standard deviation for that depth

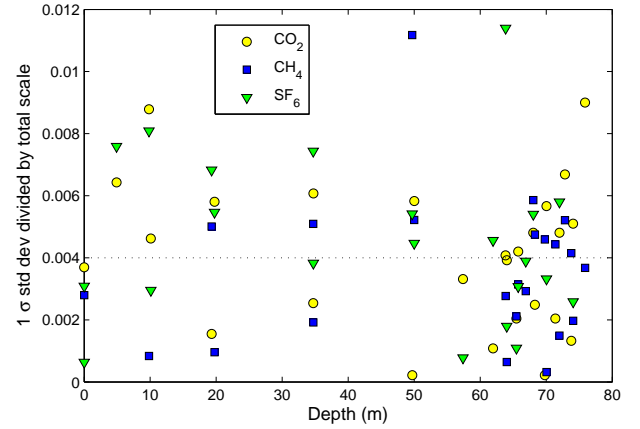


Fig. 4. Sampling uncertainties estimated from the standard deviation for each sampling depth. Standard deviations are divided by the total scale, meaning the highest measured concentration minus the lowest measured concentration.

(when available) and (2) the average sampling uncertainty as described above.

The average sampling uncertainties thus obtained are:

$$\begin{aligned} \text{CO}_2: & 0.32 \text{ ppm (EU), } 0.19 \text{ ppm (US)} \\ \text{CH}_4: & 1.8 \text{ ppb (EU), } 2.7 \text{ ppb (US)} \\ \text{SF}_6: & 0.035 \text{ ppt (EU), } 0.029 \text{ ppt (US)} \end{aligned}$$

The sampling error is found to be independent of depth (Fig. 4).

For gases where we have data from only one lab (mostly halocarbon data from the EU hole) we cannot determine the sampling errors in such a direct way. An estimate is made based on the CO_2 , CH_4 and SF_6 values given above. In Fig. 4 calculated sampling uncertainties are plotted, divided by the total signal in the firn (i.e. the highest concentration - lowest concentration). This quantity is comparable for all analysed data. The mean value (indicated by the dotted line) is 0.004. For all gases where we have only data from a single lab we used this value (0.4 % of total scale) as an estimate of sampling uncertainties.

2.7.5 Possible in-situ CO_2 artifacts

Due to the presence of organic material and (bi)carbonates in Greenland ice there is the possibility of in-situ CO_2 contamination artifacts (Tschumi and Stauffer, 2000; Guzman et al., 2007). We observe a CO_2 model-data mismatch in the deepest firn on the order of 5 ppm (Fig. 5A and Fig. 3A of the main text). For this reason we include the following uncertainty for CO_2 :

$$u_{\text{CO}_2}(z) = \begin{cases} 0 & \text{if } z < 68\text{m} \\ 0.5 \times (z - 68) & \text{if } z \geq 68\text{m} \end{cases} \quad (9)$$

This uncertainty estimate also covers the possibility of CO₂ enrichment due to close-off fractionation of the CO₂/air ratio, which occurs at the same depths (Severinghaus and Battle (2006) could not exclude a 1 ‰ effect).

In-situ cosmogenic production of ¹⁴CO₂ from nuclear spallation is known to occur (Lal et al., 1990). The production is too low by orders of magnitude to alter the CO₂ mixing ratio, however it could affect the ¹⁴CO₂ tracer. Though only the upper firn is exposed to cosmic radiation, the spallation products could be retained in the ice matrix and be released into the pore space at depth. Any in-situ ¹⁴CO₂ released into the pore space within the convective zone (top 5 m), will be lost to the atmosphere due to the vigorous ventilation. Release at lower depths would be detectable in the firn air ¹⁴CO₂ measurements. We can get an upper boundary on the ¹⁴C release by looking at the deepest samples below the ‘bomb-spike’. The deepest sample has a Δ¹⁴CO₂ of 44.9 ‰. The CO₂ mean age at this depth is from the late 1950s, for which our atmospheric reconstruction gives a atmospheric value of around 100 ‰. There is therefore no indication that the cosmogenically produced ¹⁴CO₂ has been released from the ice matrix at depth. The uncertainty related to in situ CO₂ production, however, has been translated into an uncertainty in Δ¹⁴CO₂ (~ 13 ‰ in the deepest firn).

2.7.6 Undersampling of the seasonal cycle in CO₂

The atmospheric reconstructions used in this study have a monthly resolution. In the deepest firn this is of little concern since the seasonal cycle is averaged out by the diffusion process. In the top layers undersampling of the seasonal cycle leads to a potential misfit between modeled profiles and data. We include this effect in the following way. First we linearly interpolate the CO₂ reconstruction to a $\frac{1}{2}$ month resolution. Then we run the CIC model (with nearly finalised tuning) twice, with final dates at $\pm\frac{1}{2}$ month around the firn air sampling date. The uncertainty estimate is set to half the difference between these two runs.

This test is done for all gases that vary seasonally; the effect is found to be only significant for CO₂.

2.7.7 SF₆ offset between the EU and US holes

As discussed in the main text we observe an unexplained ~ 0.25 ppt offset between the EU and US boreholes for SF₆ in the depth range $z \sim 5 - 50$ m. We can exclude differences in gas age, incomplete flask flushing, sample contamination, procedural blanks and bladder outgassing as the origin. Since we found no objective reason to reject data from either hole, we account for the discrepancy by assigning an additional errorbar to the SF₆ data from both holes. The magnitude of the assigned uncertainty is given in Table 9.

Table 9. Uncertainty estimate to account for borehole offset for SF₆. Depths on EU and US boreholes are mixed together.

Depth (m)	u_{SF_6} (ppt)
2.50	0.050
2.85	0.050
4.90	0.100
5.23	0.150
7.55	0.200
9.83	0.200
10.10	0.200
14.80	0.200
19.30	0.200
19.75	0.200
27.54	0.200
34.70	0.200
34.72	0.200
42.42	0.150
49.70	0.100
50.00	0.100
54.90	0.050

3 Modeling firn air transport at NEEM

3.1 Tuning of the diffusivity profile

3.1.1 Trace gas diffusion coefficients in air

Different trace gases have different free air diffusion coefficients (D_X^0), which result in different diffusion speeds in firn air. When the firn diffusivity profile is established for a reference gas (e.g. CO₂), it can be applied to another gas by scaling with $\gamma_X = D_X/D_{\text{CO}_2}$ (Trudinger et al., 1997). Gilliland (1934) expressed diffusion coefficients for binary gas mixtures (D_{AB}) as a function of their molecular masses (M_A , M_B) and volumes (V_A , V_B), temperature (T) and pressure (p):

$$D_{AB} = \frac{\alpha T^\beta}{p} \frac{\sqrt{1/M_A + 1/M_B}}{(V_A^{1/3} + V_B^{1/3})^2} \quad (10)$$

with $\alpha=0.0043$, and $\beta=3/2$. In the theoretical frame of Eq. (10), the γ_X diffusivity ratios are independent from temperature and pressure. Fuller et al. (1966) propose an equation similar to Eq. (10), with different values of α and β ($\alpha=0.001$, $\beta=1.75$) and new estimates of atomic and molecular volumes. However, no estimates are provided for the fluorine and bromine atoms. Massman (1998) suggest that the Chen and Othmer (1962) formula has greater predictive capabilities. Chen and Othmer (1962) proposed a semi-empirical formula developed in terms of critical temperature and molar volumes, which are available for a number of molecules (e.g. CRC, 2002):

$$D_{AB} = \frac{\alpha(T/T_0)^\beta}{(p_0/p)} \frac{\sqrt{1/M_A + 1/M_B}}{(Tc_A Tc_B/10^4)^{0.1405}} \times \frac{1}{[(Vc_A/100)^{0.4} + (Vc_B/100)^{0.4}]^2} \quad (11)$$

with $\alpha = 2.616$, $\beta = 1.81$. For most gases, diffusion coefficients in N_2 and air (and often O_2) are similar (e.g. Marrero and Mason, 1972; Matsunaga et al., 1993, 1998, 2002a, 2005, 2006, 2007, 2009).

The only exception in the Matsunaga data set is H_2 (Matsunaga et al., 2002b). Blanc's law (Blanc, 1908) is often used (e.g. Marrero and Mason, 1972) to calculate diffusion coefficients of gas X in multi-component mixtures from diffusion coefficients in binary mixtures. In the case of air, it can be written as:

$$D_{X-air}^{-1} = \frac{[O_2]}{D_{X-O_2}} + \frac{[N_2]}{D_{X-N_2}} \quad (12)$$

where $[O_2]$ and $[N_2]$ are molar fractions (e.g. 0.21 and 0.79). Matsunaga et al. (2002b) diffusion coefficients for H_2 in N_2 , O_2 and air are 6.863×10^{-5} , 7.144×10^{-5} and 6.874×10^{-5} m^2/s respectively. Equation (12) leads to 6.919×10^{-5} m^2/s in the 20.6% O_2 - 79.4% N_2 mixture used by Matsunaga et al. (2002b). It differs by 0.65% from the experimental value.

A consistent set of diffusion coefficient measurements has been published for the major greenhouse gases (Matsunaga et al., 1998), halocarbons (Matsunaga et al., 1993, 2009), SF_6 (Matsunaga et al., 2002a) and other gases with experimental precisions of about $\pm 2\%$. A comparison with previous measurements, when available, is provided as well as temperature-dependent equations fitted to the data of the form:

$$D_{AB} = \chi T^\eta \quad (13)$$

where χ and η are species-dependent scalars. As coefficient η is species-dependent, the derived γ_X ratios are slightly temperature dependent (0.2% to 1.4% in the 0 to -50° C temperature range for CH_4 , CFCs and SF_6). Measurements were performed at positive temperatures and are extrapolated to -50° C using Eq. (13) (Table 10). These data are compared with the results of the semi-empirical calculation of Chen and Othmer (1962) (%) values at 0° C in Table 10. This calculation provides better results than those from Gilliland (1934) or Fuller et al. (1966) for CFCs (Martinerie et al., 2009, Supplement). Among the 24 analysed γ_X , 18 show discrepancies between calculated and measured values $\leq \pm 3.1\%$. The 6 other species: SF_6 , CH_3Br , CH_3I , C_3H_8 , C_3H_6 and CH_3OCH_3 show distinctly higher discrepancies of 5 to 10%; these large deviations can be negative or positive.

Two other sets of relatively recent and consistent multi-species measurements are found in the literature. Results are reported only for a limited number of species (measured in firn air or in the above data set). A Canadian group performed diffusion coefficient measurements for the 3 major greenhouse gases, some halocarbons and organic species (Watts, 1971; Cowie and Watts, 1971; Barr and Watts, 1972). Lugg (1968) performed another series of measurements on some organic and halocarbon species, as well as Mercury. Lugg (1968) did not measure $D_{CO_2}^0$, thus the value from Matsunaga et al. (1998) at 25° C is used to calculate γ_X in this case. Only Watts (1971) provides temperature-dependent data, other references report measurements at 25° C. The γ_X in Table 10 are relative to the Matsunaga et al. (1998) data. It should be noted that $D_{CO_2}^0$ from Matsunaga et al. (1998) is higher than all other reported values. Deviations of the Canadian data (Watts, 1971; Cowie and Watts, 1971; Barr and Watts, 1972) from calculated values (Chen and Othmer, 1962) are variable within the range: -13.8 to $+9.5\%$. The differences between γ_X derived from Lugg (1968) and calculated values are mostly negative and range between -5.8 and $+0.2\%$.

Table 10 also shows γ_X values from two diffusion coefficient data compilations (Marrero and Mason, 1972; Massman, 1998, 1999). These compilations do not include the data set by the Matsunaga group. As the data are generally different for the various reported chemical species, the "best" $D_{CO_2}^0$ value to be used for the calculation of γ_X is unclear in the case of data compilations. Thus both values are calculated in Table 10 under the form X/Y, where X uses $D_{CO_2}^0$ from Matsunaga et al. (1998) and Y uses $D_{CO_2}^0$ from the data compilation. Deviations from the calculated values (Chen and Othmer, 1962) are somewhat similar: -6.9 to $+14.8\%$ for Massman (1998, 1999), and -10.0 to $+9.5\%$ for Marrero and Mason (1972). It should be noted than for SF_6 , the data compilation from Marrero and Mason (1972) is more consistent with the Matsunaga et al. (1998) value than with the calculated value.

Finally, the Chen and Othmer (1962) calculated γ_X are compared with the results from Bzowski et al. (1990), shown between parentheses in the last column of Table 10. Bzowski et al. (1990) used an elaborated calculation derived from the corresponding state theory to calculate diffusion coefficients in equimolar mixtures of N_2 and several gases. The resulting γ_X are always larger than those from Chen and Othmer (1962) ($+0.8$ to $+4.2\%$) and show increased differences with the data set by the Matsunaga group, except for CF_4 (the two calculated values are very close in this case: 0.8%). The Bzowski et al. (1990) calculation further increases the large discrepancy with the data obtained for SF_6 with the Chen and Othmer (1962) calculation.

Table 10. Molecular diffusion coefficient and ratios: comparison of measurements from Matsunaga et al. (1998, 2002a,b,c, 2005, 2006, 2007, 2009), a1: Barr and Watts (1972), a2: Watts (1971), a3: Cowie and Watts (1971), b: Lugg (1968), c: Massman (1998, 1999) and d: Marrero and Mason (1972) with calculated values: Chen and Othmer (1962), (Bzowski et al., 1990). D_X values are in $\text{m}^2 \text{s}^{-1}$.

X	$D_{X\text{-air}} = \chi T^\eta$	Matsunaga et al.		Other	Calc.
		γ_X at -50°C	γ_X at 0°C	γ_X at 0°C conv.	γ_X at 0°C
CO_2	$5.75 \times 10^{-10} \text{T}^{1.81}$	1	1	0.958 ^{a1} , 0.935 ^c 0.940 ^d	1
CH_4	$7.04 \times 10^{-10} \text{T}^{1.83}$	1.364	1.370 (+0.6%)	1.306 ^{a3} (-4.1%) 1.321/1.413 ^c (-3.0/+3.7%) 1.258/1.338 ^d (-7.6/-1.8%)	1.362 (1.405)
N_2O	$5.34 \times 10^{-10} \text{T}^{1.82}$	0.980	0.982 (-0.3%)	0.849 ^{a1} (-13.8%) 0.972/1.040 ^c (-1.3/+5.6%)	0.985 (1.005)
SF_6	$3.76 \times 10^{-10} \text{T}^{1.78}$	0.556	0.553 (-9.5%)	0.550/0.584 ^d (-10.0/-4.4%)	0.611 (0.625)
H_2	$41.9 \times 10^{-10} \text{T}^{1.73}$	4.73	4.650 (-3.1%)	4.521/4.807 ^d (-5.8/-0.2%)	4.799
CFC-11	$3.19 \times 10^{-10} \text{T}^{1.80}$	0.526	0.525 (+0.2%)		0.524
CFC-12	$4.77 \times 10^{-10} \text{T}^{1.75}$	0.600	0.592 (+1.2%)	0.569 ^{a1} (-2.7%)	0.585
CFC-113	$2.75 \times 10^{-10} \text{T}^{1.80}$	0.453	0.452 (+2.0%)		0.443
CFC-114	$3.97 \times 10^{-10} \text{T}^{1.75}$	0.499	0.493 (+2.7%)		0.480
CFC-115	$4.03 \times 10^{-10} \text{T}^{1.76}$	0.535	0.529 (-1.1%)		0.535
HCFC-22	$7.47 \times 10^{-10} \text{T}^{1.70}$	0.717	0.701 (+1.9%)		0.688
HCFC-123	$4.30 \times 10^{-10} \text{T}^{1.74}$	0.512	0.505 (+2.2%)		0.494
HFC-134a	$5.04 \times 10^{-10} \text{T}^{1.75}$	0.634	0.626 (+1.3%)		0.618
HFC-32	$2.72 \times 10^{-10} \text{T}^{1.92}$	0.858	0.877 (+2.8%)		0.853
HCFC-124	$3.27 \times 10^{-10} \text{T}^{1.80}$	0.539	0.538 (-0.7%)		0.542
HFC-125	$4.46 \times 10^{-10} \text{T}^{1.76}$	0.592	0.586 (-2.3%)		0.600
HFC-143a	$3.93 \times 10^{-10} \text{T}^{1.80}$	0.647	0.646 (-0.2%)		0.647
HFC-43-10mee	$2.46 \times 10^{-10} \text{T}^{1.79}$	0.384	0.382 (-0.3%)		0.383
CH_3Br	$5.57 \times 10^{-10} \text{T}^{1.76}$	0.739	0.732 (+6.9%)		0.685
CH_3I	$5.26 \times 10^{-10} \text{T}^{1.75}$	0.661	0.653 (-4.9%)		0.604
CF_4	$11.4 \times 10^{-10} \text{T}^{1.65}$	0.835	0.808 (+2.9%)		0.785 (0.791)
C_3H_8	$4.65 \times 10^{-10} \text{T}^{1.77}$	0.651	0.646 (-8.0%)	0.689 ^{a1} (-1.9%)	0.702
C_3H_6	$5.08 \times 10^{-10} \text{T}^{1.76}$	0.674	0.667 (-9.4%)		0.736
CH_3OCH_3	$6.61 \times 10^{-10} \text{T}^{1.75}$	0.831	0.821 (+10.2%)		0.745
$\text{C}_2\text{H}_5\text{OC}_2\text{H}_5$	$3.56 \times 10^{-10} \text{T}^{1.78}$	0.526	0.523 (-1.1%)	0.530 ^b (+0.2%)	0.529
CO	-	-	-	1.223/1.308 ^c (-2.2/+4.6%) 1.243/1.322 ^d (-0.6/+5.8%)	1.250 (1.303)
CH_3Cl	-	-	-	0.864 ^{a3} (+9.5%)	0.789
CHCl_3	-	-	-	0.546 ^{a2} (+4.0%), 0.519 ^{a3} (-1.1%) 0.513 ^b (-2.3%)	0.525
CH_2Cl_2	-	-	-	0.630 ^{a2} (-0.9%), 0.628 ^{a3} (-1.3%) 0.599 ^b (-5.8%)	0.636
CH_3CCl_3	-	-	-	0.459 ^b (-4.8%)	0.482
CCl_4	-	-	-	0.469 ^{a2} (-2.7%), 0.457 ^{a3} (-5.2%) 0.478 ^b (-0.8%)	0.482
Hg	-	-	-	0.822 ^b (-5.3%) 0.808/0.865 ^c (-6.9/-0.3%)	0.868
H_2O	-	-	-	1.474/1.577 ^c (+7.3/+14.8%) 1.414/1.504 ^d (+2.9/+9.5%)	1.374
N_2	-	-	-	1.210/1.295 ^c (-5.1/+1.6%)	1.275
O_2	-	-	-	1.232/1.318 ^c (-5.4/+1.2%)	1.302
C_5H_{12}	-	-	-	0.516 ^{a1} (+2.2%), 0.486 ^b (-3.8%)	0.505

3.1.2 Diffusion coefficients for trace gases and isotopic ratios at the NEEM site

The diffusion coefficient ratios γ_X for both trace gases and isotopic ratios that are used in this study are listed in Tables 11 and 12. The tables also include gases that are not directly used here, but might be of interest to fire air modeling studies in general.

We would like to add a few notes on how the diffusion coefficients were derived, and how they should be used. First, all diffusion coefficients reported here are the binary diffusivity of the gas into air. This satisfies the requirement, in order for Fick's Law of diffusion to be valid, that the gas species being modeled is diffusing into a background gas that is the major gas present. In our context, that major gas is air. The values are presented as ratios to the diffusivity of CO₂-air. Thus the values presented are unitless. This convention is followed even in the case of isotopic species.

Second, experimental values reported by the Matsunaga group are used where possible, extrapolated to -28.9°C. Where this is not possible, calculated values are given using the method of Chen and Othmer (1962). The latter are identified in Table 11 with an asterisk (*). Values for isotopic species are calculated using the “square root of the ratio of the reduced masses” law:

$$D_{X\text{-air}} = \sqrt{\frac{M_X^{-1} + M_{\text{air}}^{-1}}{M_Y^{-1} + M_{\text{air}}^{-1}}} D_{Y\text{-air}} \quad (14)$$

In what follows X generally refers to the minor isotopic species, and Y to the major isotopic species. The mass M is calculated for air by assuming that water vapor in the fire is saturated at -28.9°C, and that the mole fraction of water vapor is given by $p_{\text{H}_2\text{O}}/p$, where p is the barometric pressure of 745 mbar at NEEM. The saturation vapor pressure over ice is:

$$p_{\text{H}_2\text{O}}(\text{mbar}) = 6.1115 \exp\left[\frac{\Theta(23.036 - \Theta/333.7)}{279.82 + \Theta}\right] \quad (15)$$

where Θ is the temperature in °C. The mass of dry air is calculated from the 1976 US Standard Atmosphere (CRC, 2002), with a small adjustment for the increase in the mass of dry air due to a concentration update for the anthropogenic gases (CO₂ 385 ppm, O₂ 20.9367%, N₂ 78.088%). This results in an air mass M_{air} of 28.9589 g mol⁻¹.

Third, an isotopic substitution in a gas molecule affects the diffusivity by changing the mass. The term “isotopologue” is used for a specific isotopic species. For example, ¹²C¹⁸O¹⁶O is an isotopologue of carbon dioxide. Therefore, each isotopologue has its own value of diffusivity into air. To satisfy the above requirement for Fick's Law to be valid, each isotopologue must be modeled separately, as a trace gas diffusing into a major gas (i.e. air), each with its own diffusivity. Then, the customary delta value must be computed from the

Table 11. Diffusion coefficients of several trace gases at the NEEM site as used in this study. $T = 244.25$ K, $p = 745$ mbar. Values are based on Matsunaga et al. (1998, 2002a,b,c, 2005, 2006, 2007, 2009), unless marked with an asterisk. For those cases Eq. (11) is used (Chen and Othmer, 1962). For all these trace gases we use the natural isotopic abundance of the constituent atoms when calculating the molar mass.

Gas (X)	γ_X
CO ₂	1.000
CH ₄	1.367
N ₂ O	0.981
SF ₆	0.554
H ₂	4.694
CFC-11	0.525
CFC-12	0.596
CFC-113	0.453
CFC-114	0.496
CFC-115	0.532
HCFC-22	0.710
HCFC-123	0.509
HFC-134a	0.630
HFC-32	0.866
HCFC-124	0.538
HFC-125	0.589
HFC-143a	0.647
HFC-43-10mee	0.383
CH ₃ Br	0.736
CH ₃ I	0.658
CF ₄	0.823
C ₃ H ₈	0.649
C ₃ H ₆	0.671
CH ₃ OCH ₃	0.827
C ₂ H ₅ OC ₂ H ₅	0.525
CH ₃ CCl ₃	0.485
CCl ₄	0.470
CH ₂ Cl ₂	0.709
CHCl ₃	0.595
C ₂ H ₅ Cl	0.743
CH ₂ ClCH ₂ Cl	0.600
CH ₂ CCl ₂	0.641
CHClCCl ₂	0.583
CH ₃ Cl	0.789 *
CO	1.250 *
Hg	0.868 *
H ₂ O	1.374 *
N ₂	1.275 *
O ₂	1.302 *
C ₅ H ₁₂	0.505 *
He	4.780 *
Ne	2.140 *
Ar	1.230 *
Kr	0.962 *
Xe	0.835 *

Table 12. Diffusion coefficients for specific isotopologues. To model isotopic ratios both major and minor abundance isotopologues are to be modeled separately. Values calculated using natural abundance diffusion coefficients listed in Table 11 in combination with Eq. (14) at $T = 244.25$ K and $p = 745$ mbar.

Isotopologue (X)	γ_X	for use in
HD	3.895386	δD
HH	4.693994	δD
$^{13}CH_4$	1.340806	$\delta^{13}C$
$^{12}CH_4$	1.366969	$\delta^{13}C$
CDH ₃	1.340469 **	δD
CH ₄	1.366676 **	δD
$^{14}CO_2$	0.991368 ***	$\Delta^{14}C$
CO ₂	1.000000 †	$\Delta^{14}C$
$^{13}CO_2$	0.995613 ***	$\delta^{13}C$
$^{12}CO_2$	1.000048 ***	$\delta^{13}C$
$^{12}C^{18}OO$	0.991401	$\delta^{18}O$
$^{12}C^{17}OO$	0.995648	$\delta^{17}O$
$^{12}C^{16}OO$	1.000089	$\delta^{17}O$ and $\delta^{18}O$
$^{12}C^{18}O$	1.228754	$\delta^{18}O$
$^{12}C^{17}O$	1.239117	$\delta^{17}O$
$^{12}C^{16}O$	1.250172	$\delta^{17}O$ and $\delta^{18}O$
$^{15}NNO, N^{15}NO$	0.976915 ‡	$\alpha \delta^{15}N, \beta \delta^{15}N$
$^{18}ON_2$	0.972718	$\delta^{18}O$
$^{17}ON_2$	0.976884	$\delta^{17}O$
$^{16}ON_2$	0.981239	$\alpha \delta^{15}N, \beta \delta^{15}N, \delta^{17}O, \delta^{18}O$
^{15}NN	1.263893	$\delta^{15}N$
^{14}NN	1.275084	$\delta^{15}N$
^{18}OO	1.283719	$\delta^{18}O$
^{17}OO	1.292637	$\delta^{17}O$
^{16}OO	1.302087	$\delta^{17}O$ and $\delta^{18}O$
^{22}Ne	2.087122	$\delta^{22}Ne$ and $\delta Ne/Ar$
^{20}Ne	2.145608	$\delta^{22}Ne$
^{40}Ar	1.229952	$\delta^{40}Ar$
^{38}Ar	1.243488	$\delta^{38}Ar$
^{36}Ar	1.258324	$\delta^{40}Ar, \delta^{38}Ar, Kr, Xe, Ne$
^{86}Kr	0.958741	$\delta^{86}Kr$
^{84}Kr	0.961616	$\delta^{84}Kr$ and $\delta Kr/Ar$
^{82}Kr	0.964621	$\delta^{86}Kr$ and $\delta^{84}Kr$
^{136}Xe	0.832366	$\delta^{136}Xe$
^{132}Xe	0.834581	$\delta^{132}Xe$ and $\delta Xe/Ar$
^{129}Xe	0.836327	$\delta^{136}Xe$ and $\delta^{132}Xe$

** Includes mass effect of ^{13}C -containing isotopologue in its natural abundance, in keeping with convention for reporting deuterium data

*** Includes mass effects of ^{17}O - and ^{18}O -containing isotopologues in their natural abundances, in keeping with conventions for reporting ^{14}C and ^{13}C data (e.g. Craig (1957), Stuiver and Polach (1977))

† Convention for reporting ^{14}C has it as the ratio to non-isotopic C

‡ This value applies to both isotopomers having the ^{15}N at the central and terminal positions (Yoshida and Toyoda, 2000)

model output after the fact. For example, the $\delta^{18}O$ value for the $^{12}C^{18}O^{16}O$ isotopologue would be calculated from the outputs of two separate model runs, one for $^{12}C^{18}O^{16}O$ -air and one for $^{12}C^{16}O^{16}O$ -air:

$$\delta^{18}O = \left(\frac{[^{12}C^{18}O^{16}O]_{\text{model}}}{[^{12}C^{16}O^{16}O]_{\text{model}}} \bigg/ \frac{[^{12}C^{18}O^{16}O]}{[^{12}C^{16}O^{16}O]} \bigg|_{\text{std}} - 1 \right) \times 10^3 \quad (16)$$

where the square brackets denote a mole fraction of the isotopologue in air. The subscript ‘model’ refers to mole fractions as calculated by the model, and the subscript ‘std’ refers to the ratio of mole fractions of the reference standard used for reporting the delta value (here, this would be V-PDB).

Fourth, to relate the values of diffusivities for isotopic species to the values for non-isotopic gases (e.g. mixtures of different isotopes in their natural abundance) in an internally consistent way, we calculated the ratio of the diffusivity of gas Y (the major isotopologue) to the diffusivity of the non-isotopic species NI using the equation:

$$\frac{D_{Y\text{-air}}}{D_{NI\text{-air}}} = \sqrt{\frac{M_Y^{-1} + M_{\text{air}}^{-1}}{M_{NI}^{-1} + M_{\text{air}}^{-1}}} \quad (17)$$

The mass of the non-isotopic species M_{NI} for this purpose was the natural abundance mass (an abundance-weighted average of the masses of all the isotopes). This ratio was then multiplied by the value of D_{NI}/D_{CO_2} for the non-isotopic species (typically an experimental value), to produce the final values of D_Y/D_{CO_2} for the major, and D_X/D_{CO_2} for the minor isotopologue:

$$\gamma_Y = D_Y/D_{CO_2} = \frac{D_{Y\text{-air}}}{D_{NI\text{-air}}} \times D_{NI}/D_{CO_2} \quad (18)$$

$$\gamma_X = D_X/D_{CO_2} = \frac{D_{X\text{-air}}}{D_{Y\text{-air}}} \times D_Y/D_{CO_2} \quad (19)$$

The differences between D_Y and D_{NI} are not significant in most cases, but we nonetheless calculated them for the sake of conceptual clarity. For example, the value of D_Y/D_{CO_2} for the isotopologue $^{12}C^{16}O^{16}O$ is 1.000089, compared with the value of D_{NI}/D_{CO_2} of 1.000000 (by definition). The reason that the natural-abundance isotopic mixture diffuses slightly more slowly than the isotopologue $^{12}C^{16}O^{16}O$ is that the mixture contains trace amounts of heavier isotopologues such as $^{13}C^{16}O^{16}O$.

Fifth, the non-isotopic species are generally not used to calculate delta values ($\Delta^{14}C$ is an exception). Rather, the species in the denominator in the delta calculation is generally a specific isotope, usually the major isotope, such as 1H , ^{12}C , ^{14}N , or ^{16}O . Also, Table 11 only presents three or four significant figures for the diffusivities for non-isotopic species. This is not usually sufficient for delta calculations. So all δ calculations should use the diffusivities in Table 12,

which have 6 or 7 significant figures. Of course, the absolute values are not that well known, but the relative values of a pair are quite well known, as the relative values depend only on Eq. (14).

Sixth, the convention for reporting isotopic data usually includes all isotopologues containing a certain isotope, not just the most abundant one. For example, $\delta^{13}\text{C}$ is defined as:

$$\delta^{13}\text{C} = \left(\frac{^{13}\text{C}}{^{12}\text{C}} \Big|_{\text{sample}} / \frac{^{13}\text{C}}{^{12}\text{C}} \Big|_{\text{V-PDB}} - 1 \right) \times 10^3 \quad (20)$$

For CO_2 , the numerator here would include the sum of the abundances of not only $^{13}\text{C}^{16}\text{O}^{16}\text{O}$, but also $^{13}\text{C}^{17}\text{O}^{16}\text{O}$, $^{13}\text{C}^{18}\text{O}^{16}\text{O}$, $^{13}\text{C}^{18}\text{O}^{18}\text{O}$, etc. The denominator would include $^{12}\text{C}^{16}\text{O}^{16}\text{O}$, $^{12}\text{C}^{17}\text{O}^{16}\text{O}$, $^{12}\text{C}^{18}\text{O}^{16}\text{O}$, $^{12}\text{C}^{18}\text{O}^{18}\text{O}$, etc. Although it is impractical to measure all the minor ^{13}C -containing isotopologues with mass spectrometry, a correction is routinely applied that approximately accounts for all of these (the ^{17}O correction; Craig (1957)). Similarly, chemical transformations often bring all the various forms of isotopes into a single isotopologue, as part of a routine analysis. For example, H_2 gas is produced chemically during the analysis of deuterium/hydrogen ratios in methane. For this reason the mass used to calculate diffusion coefficients should be a weighted average of the various isotopologues that exist, which will ultimately contribute to the analysis.

We account for this effect in several cases, marked with asterisks. In other cases we neglect it as the abundances are too small to be significant (for example, ^{13}C is relatively abundant at 1 in 100 carbon atoms, so we account for it, but deuterium is extremely rare at 1 in 6500 hydrogen atoms, so we neglect its effect on the weighted average mass). In still other cases we neglect it because the precision of the measurements is far too low for this issue to matter (e.g., $^{15}\text{N}_2\text{O}$).

3.2 Model description

Below follows a brief description of the different firn air models in alphabetical order.

3.2.1 CIC model

The CIC firn air model is a finite difference 1-D diffusion model coded in MATLAB. It uses implicit Crank-Nicholson timestepping to solve what is essentially an advection-diffusion-reaction equation, with radioactive decay and bubble trapping taking the place of the chemical reaction by removing trace gas molecules from the open pore space. The model uses a stationary reference frame with $z = 0$ at the surface. The firn column is assumed to be isothermal and in steady state with regard to ice flow and densification rates.

The model includes four types of transport in the open porosity. The first type is molecular diffusion, which is included through the effective molecular diffusion coefficient D_X , where the X denotes the trace gas under consideration.

The second type is gravitational settling, which tends to enrich the firn in heavier molecules with depth (Sowers et al., 1992). The third type is advection, which we include through an average downward velocity of the air in the open pores w_{air} . The fourth type of transport is an eddy diffusion. It describes mass transfer caused by macroscopic flow patterns in the open porosity which the model cannot resolve directly, and are instead parameterised through the inclusion of an eddy diffusion coefficient D_{eddy} . Two effects were included as an eddy diffusivity. First, we use the parameterisation by Kawamura et al. (2006) to describe wind pumping and convection in the top firn layers (Colbeck, 1989). Second, we include dispersive mixing in the LIZ. Using a molecular diffusivity in the LIZ instead would lead to continued gravitational enrichment with depth, which contradicts observations.

The flux of a trace gas X in the firn is described by

$$J_X = -D_X \left(\frac{\partial C}{\partial z} - \frac{\Delta M g C}{RT} \right) - D_{\text{eddy}} \frac{\partial C}{\partial z} + w_{\text{air}} C \quad (21)$$

where C is the mixing ratio of the trace gas, $\Delta M = M_X - M_{\text{air}}$ the molar mass deviation from dry air in kg mol^{-1} , g the gravitational acceleration, R the molar gas constant and T the firn temperature in K .

Imposing mass conservation gives

$$\frac{\partial C}{\partial t} = \frac{1}{s_{\text{op}}^*} \frac{\partial}{\partial z} (s_{\text{op}}^* J_X) - \lambda_X C - \theta C \quad (22)$$

where λ_X is the radioactive decay constant in s^{-1} , θ is the bubble trapping rate in s^{-1} and s_{op}^* is the effective open porosity

$$s_{\text{op}}^* = s_{\text{op}} \exp \left[\frac{M_{\text{air}} g z}{RT} \right] \quad (23)$$

i.e. the open porosity corrected for the barometric pressure increase with depth in the firn.

To implement Eq. (22) in a numerical scheme it is split up in the different derivatives in C .

$$\frac{\partial C}{\partial t} = b_1 \frac{\partial^2 C}{\partial z^2} + b_2 \frac{\partial C}{\partial z} + b_3 C \quad (24)$$

with

$$b_1 = D_X + D_{\text{eddy}} \quad (25)$$

$$b_2 = -D_X \frac{\Delta M g}{RT} + \frac{1}{s_{\text{op}}^*} \frac{d}{dz} [s_{\text{op}}^* (D_X + D_{\text{eddy}})] - w_{\text{air}} \quad (26)$$

$$b_3 = -\frac{1}{s_{\text{op}}^*} \left(\frac{\Delta M g}{RT} \frac{d}{dz} (s_{\text{op}}^* D_X) + \frac{d}{dz} (s_{\text{op}}^* w_{\text{air}}) \right) - \lambda_X - \theta \quad (27)$$

We now consider conservation of air in the open and closed porosity, from which we can derive the average downward velocity in open pores w_{air} and the trapping rate θ . The air flux in the open and closed porosities is given as

$$\phi_{\text{op}} = s_{\text{op}}^* w_{\text{air}} \quad (28)$$

$$\phi_{\text{cl}} = s_{\text{cl}} \frac{p_{\text{cl}}}{p_0} w_{\text{ice}} = s_{\text{cl}} \frac{p_{\text{cl}}}{p_0} A \frac{\rho_{\text{ice}}}{\rho} \quad (29)$$

where the fraction p_{cl}/p_0 is the enhanced pressure in the closed porosity relative to the surface pressure due to compression of bubbles during firn densification.

Conservation of mass in combination with our assumption of steady state gives $\forall z$:

$$\phi_{\text{op}}(z) + \phi_{\text{cl}}(z) = \phi_{\text{cl}}(z_{\text{COD}}) \quad (30)$$

where z_{COD} is the full close-off depth where all the air is occluded in bubbles ($s_{\text{op}}(z_{\text{COD}}) = 0$). What Eq. (30) says is that at each depth the total flux of air must be equal, and that the total flux is given by ϕ_{cl} at close-off. From Eq. (30) we can solve for the air velocity in the open pore space:

$$w_{\text{air}} = \frac{A \rho_{\text{ice}}}{s_{\text{op}}^* p_0} \left(\frac{s_{\text{cl}}(z_{\text{COD}}) p_{\text{cl}}(z_{\text{COD}})}{\rho_{\text{COD}}} - \frac{s_{\text{cl}}(z) p_{\text{cl}}(z)}{\rho(z)} \right) \quad (31)$$

We see that w_{air} depends solely on the accumulation rate and the firn structure.

The flux in the open porosity (Eq. (28)) decreases with depth. This is because of the trapping process which continuously removes air from the open porosity. From considerations of mass conservation we can derive the trapping rate to be:

$$s_{\text{op}}^* \theta = - \frac{d}{dz} (s_{\text{op}}^* w_{\text{air}}) \quad (32)$$

On inserting Eq. (32) into Eq. (27) we obtain:

$$b_3 = - \frac{\Delta M g}{RT} \frac{1}{s_{\text{op}}^*} \frac{d}{dz} (s_{\text{op}}^* D_X) - \lambda_X \quad (33)$$

We see that the trapping rate has fallen out of the equations altogether. This is to be expected, since the trapping process does not alter the mixing ratios in the open porosity (here we neglect molecular size dependent bubble close-off fractionation (Huber et al., 2006; Severinghaus and Battle, 2006)).

The only unknown parameter in Eq. (31) is the pressure build-up p_{cl}/p_0 in the closed porosity. This influences the velocity in the open pores, as well as the total air content of the ice below close-off. The total compression includes two terms. First, we assume that the densification process reduces the closed porosity equally to the total porosity. In the closed

pores this leads to bubble compression and pressure build-up, whereas in the open pores it leads to gas expulsion into overlying firn layers. This assumption is reasonable since the overburden pressure that causes the firn to compact is many times larger than the pressure in the closed pores (p_{cl}/p_0 goes to 1.3 for the method presented here). Second, we include compaction due to the negative strain rates $\dot{\epsilon}_{zz} = dw_{\text{ice}}/dz$ in the firn. This causes annual layers to approach each other, compressing the air as well.

We let an ice parcel sink down into the firn from z' to z . A bubble that is first trapped at depth z' will travel down with the ice, and when it reaches depth z its pressure will have increased by a factor

$$\xi(z', z) = \frac{s(z')/s(z)}{1 + \int_{z'}^z \dot{\epsilon}_{zz}/w_{\text{ice}} dz''} \quad (34)$$

where the numerator describes the contribution of densification, and the denominator the contribution of the negative strain rates. The closed porosity at depth z is a mixture of bubbles trapped along the depth range $0-z$. Thus for $z \leq z_{\text{co}}$ the mean bubble pressure is given by

$$\frac{p_{\text{cl}}(z)}{p_0} = \int_0^z \frac{ds_{\text{cl}}}{dz'} \exp\left(\frac{M_{\text{air}} g z'}{RT}\right) \xi(z', z) dz' \quad (35)$$

and for $z > z_{\text{COD}}$ we get

$$\frac{p_{\text{cl}}(z)}{p_0} = \frac{p_{\text{cl}}(z_{\text{COD}})}{p_0} \xi(z_{\text{COD}}, z) \quad (36)$$

The correctness of these equations is easily verified by calculating the closed flux ϕ_{cl} using Eq. (29). Indeed for $z > z_{\text{COD}}$ we find a constant flux, as required by mass conservation.

The total air content of the ice can be calculated as

$$x_{\text{air}} = 1000 \times s_{\text{cl}}(z_{\text{COD}}) \frac{p_{\text{cl}}(z_{\text{COD}})}{p_0} \frac{p_0}{101325} \frac{273.15}{T} / \rho_{\text{COD}} \quad (37)$$

where x_{air} is the total air content in mL STP air per kg of ice. For NEEM we find $x_{\text{air}} = 100.9$ mL STP air per kg ice. Unfortunately we have no accurate air content measurements to verify this number.

Finally we turn to the tuning procedure. We tune the inverse tortuosity profile $\tau^{-1}(z)$; the effective molecular diffusivity is given as $D_X(z) = D_X^0 \tau^{-1}(z)$. As an initial guess for $\tau_0^{-1}(z)$ we use the parameterisation by Schwander (1989). The optimal diffusivity for NEEM can be written as

$$\tau^{-1}(z) = \tau_0^{-1}(z) \times [1 + f(z)] \quad (38)$$

where $f(z)$ is a smooth function which we will try to estimate in the tuning procedure. We construct $f(z)$ from its Fourier components

$$f(z) = c_0 + \sum_{n=1}^N \left[c_n \sin\left(\frac{n\pi z}{2L}\right) + d_n \cos\left(\frac{n\pi z}{2L}\right) \right] \quad (39)$$

where L is the total length of the open porosity firn column (78 m), and N determines the smoothness of the final diffusivity profile. The optimal values of the coefficients c_n and d_n are found in an automated gradient method. For the tuning of NEEM a value of $N = 20$ was used. We set $\max[\tau^{-1}(z)] = 1$, i.e. the diffusivity in the firn cannot exceed the free-air diffusivity. It was found that including other functions $f_i(z)$, such as linear slopes $f_i(z) = z/L$, tends to speed up the convergence to the final solution. More details will be given elsewhere.

3.2.2 CSIRO model

The CSIRO firn model is based on the model described by Trudinger et al. (1997). Since then it has been rewritten into Fortran90, flux smoothing is no longer used, and an implicit timestepping, the same as that used by Rommelaere et al. (1997), has replaced the Euler predictor-corrector scheme. The timestep used here was 0.1 years up to 2000 then 0.01 years to the end. An exponential eddy diffusion flux has been added following Severinghaus et al. (2001) to account for convective mixing near the surface, with 2 tuned parameters (surface magnitude and scale depth). A key difference between the CSIRO firn model and the other models is that it neglects the upward flux of air due to compression of pore space. A genetic algorithm (from Haupt and Haupt (1998)) is used to calibrate the diffusivity versus open porosity and the eddy diffusion parameters. We adjust the open porosity values corresponding to about 12 specified diffusivity values to give the diffusivity profile, with cubic splines used to interpolate between these points, and diffusivity capped at $500 \text{ m}^2 \text{ yr}^{-1}$ ($0.158 \times 10^{-4} \text{ m}^2 \text{ s}^{-1}$) near the surface. We only allow monotonic solutions (as defined by the points) but the cubic splines, which match the gradient of adjacent splines at each point, can often lead to non-monotonic diffusivity vs open porosity profiles. We therefore penalise oscillatory behaviour with an additional term added to the cost function that is the squared difference between a line integral following the cubic spline and a line integral for linear interpolation between the points. Any negative diffusivity values are set to zero. The best solution for the NEEM EU hole had the diffusivity going to zero then increasing above zero below this. This was not intentional, but was caused by the cubic splines. The US case did not generate the same behaviour, instead the best fit was obtained with diffusivity that decreased to zero at about 63 m. The genetic algorithm does not require an initial guess, but does require a range for each parameter. The ranges were initially chosen as representative of values for other calibrated sites, and extended if solutions from the genetic algorithm with low values of the cost function collected

near either end of the range. More detail on the calibration method will be given in Trudinger et al. (in preparation).

3.2.3 INSTAAR model

The INSTAAR one-dimensional firn gas transport model was originally based on a model described in Severinghaus and Battle (2006), but has evolved substantially. The model has fixed coordinates with only the gases moving through the firn matrix. The firn matrix is considered to be in steady state. The NEEM firn is parameterised with 1 m deep boxes between -0.5 and 59.5 m (top model box is half-free air, half-firn), and with 0.25 m deep boxes below 59.5 m.

Gases are moved through the firn by four mechanisms: (1) molecular diffusion (different for different gases), (2) gravitational settling, (3) eddy diffusion or turbulent mixing (same for all gases), (4) downward advection (same for all gases). For each box, the model keeps track of the gas content in the open porosity as well as in the ice-enclosed bubbles, but the gas mixing ratios are only tracked in the open porosity part. Rate of total downward air advection is determined from the air content of ice below close-off and the ice accumulation rate. From mass conservation, the total downward air advection should be the same at each level. The rate of advection in the open porosity at each level is therefore calculated as the total downward air advection rate minus the advection of air in the bubbles at that level (found from bubble air content and ice accumulation rate).

Unlike the model described in Severinghaus and Battle (2006), the INSTAAR model does not have any fundamental differences in the mechanisms of gas movement between the diffusive zone and the lock-in zone. In the INSTAAR model the reduced gas movement in the lock-in zone is achieved simply through adjusting the overall effective gas diffusivities to lower levels.

The model includes a seasonal temperature cycle and calculates firn temperature in each model box in the same way as the Severinghaus and Battle (2006) firn model.

The model uses explicit time stepping. To avoid computational instability the time step is always chosen to be smaller than $\Delta t < (\Delta z)^2 / 3D_{\text{total}}$, where Δt is the time step, Δz is the box size in m, and D_{total} is the total effective diffusivity in $\text{m}^2 \text{ s}^{-1}$. For all gases except H_2 , this time step was set to 11,119 s (3.5×10^{-4} yr). For H_2 , which has a much higher molecular diffusivity, the time step was set to 3,156 s (1×10^{-4} yr).

The equation used to calculate flux of gas X between two adjacent boxes due to molecular diffusion and gravity at each time step is as follows:

$$J_{X;\text{molec-grav}(i)} = -\gamma_X D_{\text{CO}_2}^0 \tau_i^{-1} s_{\text{op}; \text{mid}} \times \left(\frac{C_{i+1} - C_i}{\Delta z_{\text{mid}}} - \frac{\Delta M g}{RT_i} \frac{C_{i+1} + C_i}{2} \right) \quad (40)$$

Here $J_{X;\text{molec-grav}(i)}$ is the gas flux between box i and $i+1$ (in units of e.g., $\text{ppmm}^3\text{m}^{-2}\text{s}^{-1}$). This can be thought of as the volume of the pure gas moving across a unit area of the boundary between boxes per unit time. $\gamma_X D_{\text{CO}_2}^0$ is the free-air diffusivity of gas X at the boundary between box i and $i+1$ in m^2s^{-1} , re-calculated at each time step to take into account firn temperature variations; τ_i^{-1} is the tuned dimensionless multiplier (or inverse tortuosity) to the free air diffusivity for box i . $s_{\text{op};\text{mid}}$ is the open porosity (m^3/m^3) at the boundary between the two boxes. This is included because the flux should be proportional to the open porosity. C_i is the gas mixing ratio in box i (e.g., in ppm), Δz_{mid} is the distance (m) between the middles of box i and box $i+1$, ΔM is the molar mass difference (kgmol^{-1}) between the gas and bulk air, g is the acceleration due to gravity (ms^{-2}), R is the universal gas constant ($\text{Jmol}^{-1}\text{K}^{-1}$) and T_i is the firn temperature (K) at the boundary between boxes i and $i+1$.

The basic form of the equation used to calculate the gas flux due to eddy diffusion or turbulent mixing is:

$$J_{\text{eddy}(i)} = -D_{\text{eddy}(i)} s_{\text{op};\text{mid}} \frac{C_{i+1} - C_i}{\Delta z_{\text{mid}}} \quad (41)$$

where $J_{\text{eddy}(i)}$ is the gas flux due to eddy diffusion ($\text{ppmm}^3\text{m}^{-2}\text{s}^{-1}$) and $D_{\text{eddy}(i)}$ is the tuned eddy diffusivity (m^2s^{-1}) for box i .

Gas fluxes due to advection and flux of air into newly formed bubbles are also calculated at each time step. All of these fluxes are corrected to STP volumes (to account for varying temperature and pressure in the firn column) and are added to find the total flux of gas into the box (J_{in}) and the total flux of gas out of the box (J_{out}). The time derivative of the gas mixing ratio in box i is then calculated as:

$$\frac{\Delta C_i}{\Delta t} = \left(\frac{J_{\text{in}} - J_{\text{out}}}{s_{\text{op}(i)} \Delta z_i} \right) \quad (42)$$

where s_i is the open porosity in the box and Δz_i is the vertical length of box i .

The effective diffusivities in the INSTAAR model were manually tuned to optimise the fit to the suite of 10 gases. The initial guess for effective molecular diffusivities used the free-air diffusivity in the surface box, with effective diffusivities for CO_2 declining linearly to $2.0 \times 10^{-9} \text{ m}^2\text{s}^{-1}$ at 64m and staying constant beyond 64 m. The initial guess for eddy diffusivity set the eddy diffusivity equal to molecular diffusivity for CO_2 in the surface box, and prescribed an exponential decrease with depth using an e-folding depth of 4 m. Below the depth where eddy diffusivity dropped to $1.0 \times 10^{-8} \text{ m}^2\text{s}^{-1}$ it was held constant at this value.

3.2.4 LGGE-GIPSA model

In the LGGE-GIPSA model (Witrant et al., in preparation for this issue), the transport processes described in (Rommelaere et al., 1997) have been revised in a poromechanics framework, where the ice lattice, the gases in open pores and

the gases in closed pores are considered as an interconnected network constrained by mass conservation. The model dynamics is expressed in terms of densities and the diffusion process is described as a combination of Fick's and Darcy's transport, thus allowing to distinguish between a purely diffusive transport (molecular and eddy) in the convective layer and an almost-stagnant transport in the lower zones. The numerical implementation is done with an implicit time discretization with a one week step and combined central/Lax-Wendroff space discretization with a step of 0.2 m.

Firn diffusivity is calculated using a constrained non linear least square multi-gas optimization scheme, with the optimisation problem formulated by Witrant and Martinerie (2010). $\delta^{15}\text{N}_2$ was not used for diffusivity optimisation but kept for the physical model transport validation. By contrast with some of the other models in this intercomparison, only molecular diffusivity (no eddy-diffusivity) is considered in the deep firn. An eddy diffusion term (D_{eddy}) is taken into account in the upper firn to represent convective transport: when firn diffusivity calculated by our optimisation procedure exceeds the speed of molecular diffusion in free air D_X^0 corrected by a factor α to take into account the porosity effect (Severinghaus and Battle, 2006), the firn diffusivity is calculated as $\alpha D_X^0 + D_{\text{eddy}}$. D_{eddy} is then the quantity tuned by our least square multi-gas optimisation in order to best fit the firn data. No pre-defined depths are used to constrain the limits of the convective and lock-in zone except for the depth at which gravitational fractionation starts (set as 4 m for NEEM). The lower boundary for gravitational fractionation (lock-in depth) is calculated by the model.

The model has been evaluated on 12 additional Arctic (Devon Island, North GRIP, Summit) and Antarctic (DE08, Berkner Island, Siple Dome, Dronning Maud Land, South Pole 1995, South Pole 2001, Dome C, Vostok) previously simulated with the Rommelaere et al. (1997) model.

3.2.5 OSU model

The OSU firn air model is a finite-difference diffusion model based on the mixing ratio equations of Trudinger et al. (1997), Eqs. (A9) and (A13). However, the OSU model differs from this model in the following ways. First, an eddy-diffusion term is added to represent surface convection, based on the parameterisation of Kawamura et al. (2006), and also to account for the necessary mixing that is observed within the LIZ but cannot be due to molecular diffusion.

Second, the model uses an implicit Crank-Nicholson numerical scheme, which makes it stable over a large range of depth increments and time steps. Because of this, at the model time step of 0.005 years and depth resolution of 0.1 m, the flux smoothing technique of Trudinger et al. (1997) is not employed.

Lastly, vertical advection of the firn is accounted for by shuffling boxes down at every time step, rather than moving the reference frame (Schwander et al., 1993). An evenly

spaced depth scale is used, which makes computation of the diffusion equation simpler but complicates shifting boxes as the firn densifies and the equally spaced boxes contain less and less air. To deal with this, the vertical displacement of the air at every depth and every time step is calculated. The vertical air velocity used to compute displacement differs from the ice velocity (Rommelaere et al., 1997) and is given by the equation of Buizert (Eq. (31)). This creates a new mixing-ratio profile with different depth values which is then interpolated back onto the fixed grid, and assigned the correct firn properties at each depth. The value of the top box is set to the atmospheric mixing ratio for the current time step during this process.

Bubble compression is accounted for only in the LIZ, because above this zone it is assumed that the pressure in the open porosity is equal to atmospheric pressure. Below the top of the LIZ, the model uses the following correction to account for the greater amount of air in the open porous volume:

$$s_{\text{op}}^*(z) = s_{\text{op}}(z) \frac{\rho(z)}{\rho_{\text{LID}}} \quad (43)$$

where $s_{\text{op}}(z)$ is the true open porosity at depth z (Eq. (4)), $\rho(z)$ is the density (Eqs. (1-3)), and ρ_{LID} is the density at the lock-in depth, i.e. at the top of the LIZ. Bubble compression of the closed porosity is ignored since this is an open porosity model. The free air diffusivity of CO_2 ($D_{\text{CO}_2}^0 = 1 \times 10^{-5} \text{ m}^2\text{s}^{-1}$) is first corrected for site temperature and pressure (Schwander et al., 1988), then adjusted for depth based on the porosity (note that this is based on the actual porosity, not the effective porosity defined above). The diffusivity parameterisation of Schwander et al. (1993) is used as a first estimate, but a second-order porosity dependence was added later to improve the fit. The form of the final diffusivity profile is:

$$D_X(z) = D_X^0 [g_1 + g_2 s_{\text{op}}(z) + g_3 s_{\text{op}}^2(z)] \quad (44)$$

Values for constants g_1 , g_2 and g_3 were manually adjusted to minimise the total root mean squared error of the model-data mismatch for all tracers, including $\delta^{15}\text{N}$. Final values are listed in Table 13. Where molecular diffusivity goes to zero in the LIZ, the model uses a synthetic exponential decrease to prevent numerical instabilities. This takes the form:

$$D_X(z) = g_4 + (D_X(z_{\text{LID}}) - g_4) e^{-g_5(z - z_{\text{LID}})}, \quad \text{for } z > z_{\text{LID}} \quad (45)$$

where g_4 is some relict molecular diffusivity and z_{LID} is the lock-in depth. Dispersive eddy diffusivity in the lock-in zone is parameterised by the following exponential:

$$D_{\text{eddy}}(z) = g_6 e^{g_7(z - z_{\text{LID}})}, \quad \text{for } z > z_{\text{LID}} \quad (46)$$

where again g_6 and g_7 were iteratively adjusted to provide the best fit to the data.

Table 13. Constants used in the OSU diffusivity tuning for the EU borehole

constant	value	unit
g_1	- 0.209	
g_2	1.515	
g_3	0.53	
g_4	3.17×10^{-10}	m^2s^{-1}
g_5	1.82	m
g_6	3.17×10^{-9}	m^2s^{-1}
g_7	0.11	m

3.2.6 SIO model

The Scripps Institution of Oceanography (SIO) firn air model follows generally those of Schwander et al. (1993), Rommelaere et al. (1997), Severinghaus and Battle (2006), and Severinghaus et al. (2010) (hereafter S2010). Slight differences from the model of S2010 include the following. (i) Barometric pressure increases with depth, according to the isothermal barometric equation set with the initial mean-annual temperature, (ii) gravity is set to zero within the lock-in zone, (iii) molecular and eddy diffusion both continue throughout the LIZ, and (iv) the LIZ grid spacing is calculated with the air advection velocity until the close-off density (Martinerie et al., 1992) and thereafter with the firn velocity, whereas S2010 calculated it with the firn velocity in the entire LIZ.

The main differences between the SIO model and the other models in the present intercomparison are:

1) The model has a parallel heat transport model within it that predicts temperature as a function of depth and time. Using these temperatures, the model computes fractionation of gases and isotopes by thermal diffusion, gravitational settling, and temperature-sensitive kinetic disequilibrium processes. Disequilibrium arises from convection in the near-surface layers, downward advection due to snow accumulation and bubble close-off, and transients in atmospheric gas mixing ratios and temperatures. For the NEEM intercomparison runs, the temperature model was disabled, but the full model was used to make thermal diffusion corrections to NEEM firn air $\delta^{15}\text{N}$ and $\delta^{86}\text{Kr}$ data used as inputs.

2) The SIO model treats downward air advection in the LIZ by shifting concentrations down by one grid point every 0.5 yr, rather than with explicit advection schemes. The grid points are spaced apart by distances such that the air advection velocity w_{air} would transport the air that distance in 0.5 yr. This scheme minimizes the numerical diffusion common to upwind advection schemes. As a result, the SIO model has the highest mixing ratio of tracer (oldest gas) in its lock-in zone in Diagnostic Test 4. This lack of numerical diffusion also implies that the diffusivities found by tuning to observed gas profiles should be slightly higher than those

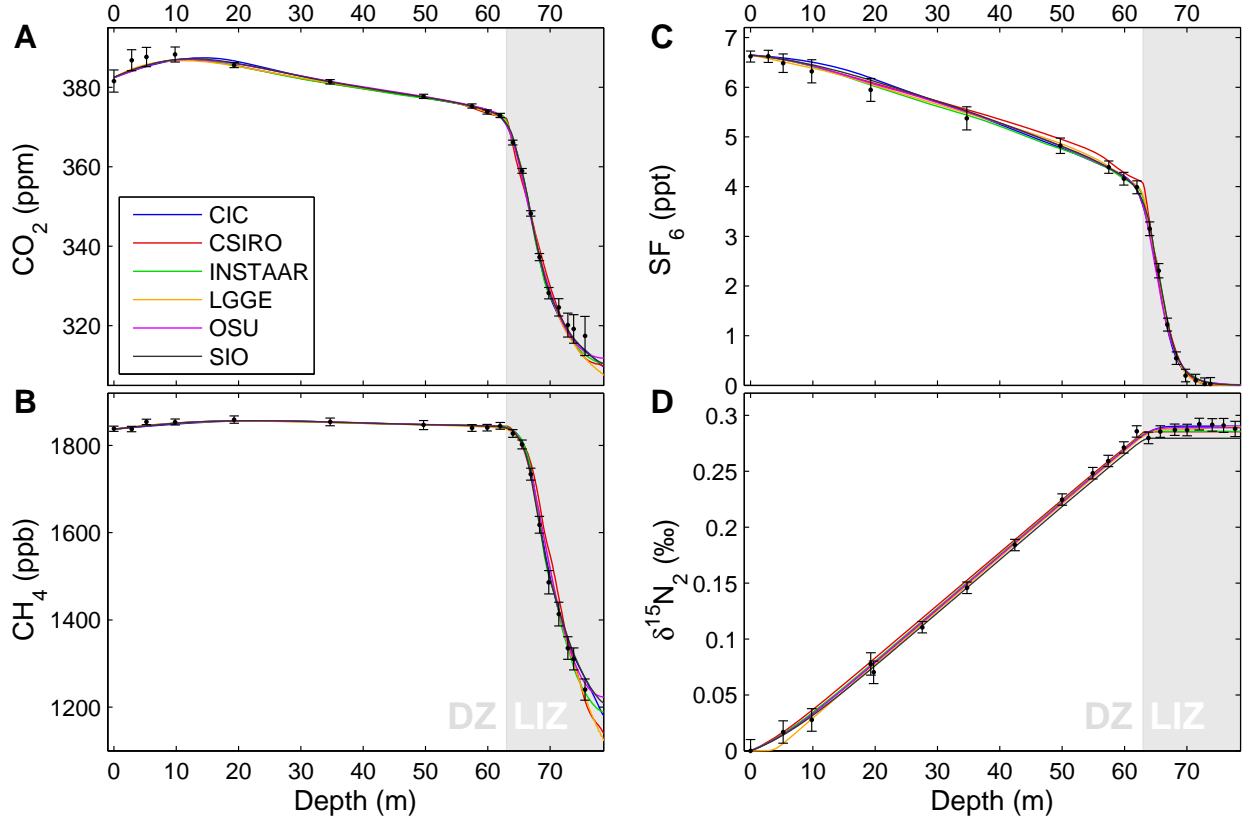


Fig. 5. (A-D) Modeled profiles for all 4 tracers from the US borehole. With the exception of (D) data has been gravity corrected and the models are run with gravity turned off. Errorbars correspond to full 1σ uncertainty as defined in Sect. 2.7.

of the other models. This lock-in zone architecture was chosen so that second derivatives of atmospheric variations in trace gases would be preserved within the lock-in zone to the extent possible. For example, the dip in atmospheric CO_2 in the early 1940s can be preserved by the SIO model given a sufficiently high accumulation rate. The diffusion correction for $^{13}\text{CO}_2$ and $^{13}\text{CH}_4$ is also arguably more accurate with a minimum of numerical diffusion.

The inverse tortuosity profile $\tau^{-1}(z)$ is tuned using a generalised least square method. The initial guess $\tau_o^{-1}(z)$ is the parameterisation by Schwander (1989). Subsequent profiles are determined using:

$$\tau^{-1}(z) = \tau_o^{-1}(z) + \sum_{i=1}^N h_i * f_i(z) \quad (47)$$

$$\begin{aligned} f_i(z) &= 0 & z < i\Delta z \\ f_i(z) &= a(z - i\Delta z) / \Delta z & i\Delta z < z < (i+1)\Delta z \\ f_i(z) &= a((i+2)\Delta z - z) / \Delta z & (i+1)\Delta z < z < (i+2)\Delta z \\ f_i(z) &= 0 & z > (i+2)\Delta z \end{aligned}$$

We use an amplitude $a = 10^{-6} \text{ m}^2\text{s}^{-1}$ between 0 and 60m, and $a = 10^{-8} \text{ m}^2\text{s}^{-1}$ between 60 and 80m. The half width Δz was set to $\Delta z = 0.5 \text{ m}$. The coefficients h_i are optimised using a least square regression to minimise the RMS misfit given in Eq. (3) of the main text.

Near the surface, the eddy diffusivity due to wind pumping is parameterised by an exponential:

$$D_{\text{eddy}}(z) = D_{\text{eddy}}^0 \exp\left(-\frac{z}{H}\right) \quad (48)$$

$D_{\text{eddy}}^0 = 1.6e^{-5} \text{ m}^2\text{s}^{-1}$ and $H = 5 \text{ m}$ are tuned to fit the $\delta^{15}\text{N}$ and $\delta^{86}\text{Kr}$ data, corrected for thermal fractionation.

In the lock in zone, the balance between molecular diffusion (affecting each gas differently) and dispersion (affecting all the gases proportionally) is determined by a single coefficient α varying between 0 and 1, rather than by having a free dispersion diffusivity profile, which is largely unconstrained. The molecular diffusivity is then:

$$D_X(z) = (1 - \alpha) \frac{D_X^0}{\tau(z)} \quad (49)$$

And the dispersion, included as an eddy diffusivity, is:

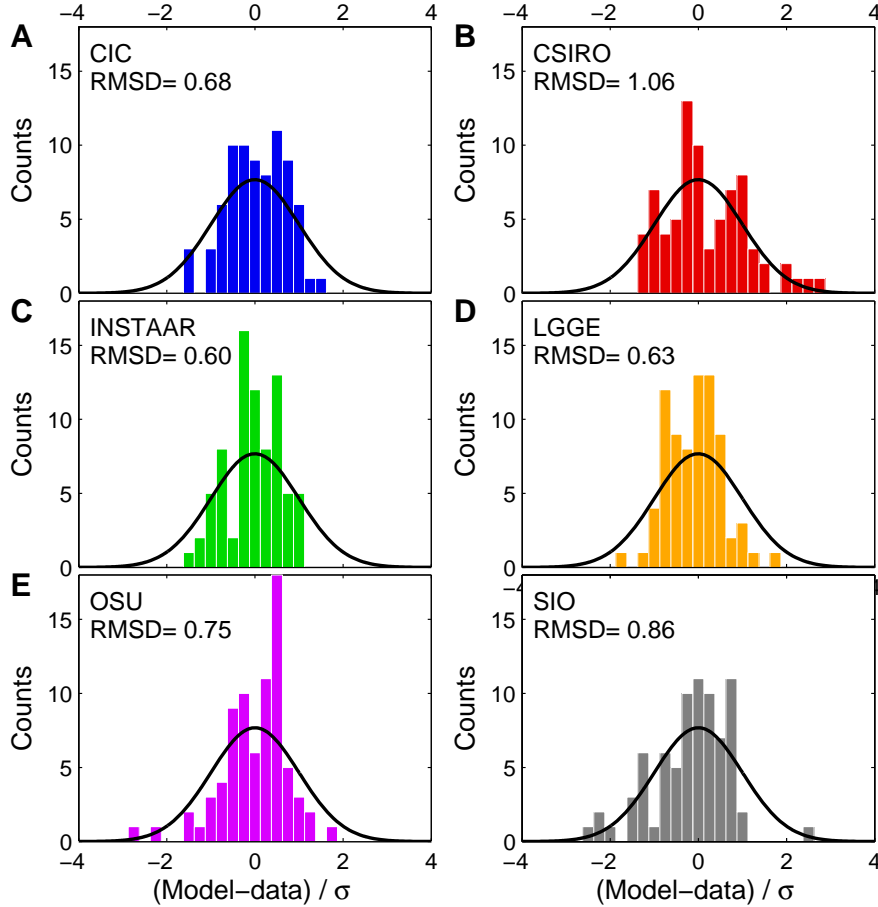


Fig. 6. (A-E) Histogram of $(m_i - d_i)/\sigma_i$ for the firn air transport models in this study using the US borehole data. The black curve gives a Gaussian distribution of width $\sigma = 1$, normalised to have equal surface to the histogram. The RMSD is calculated with Eq. (3) of the main article.

$$D_{\text{eddy}}(z) = \alpha \frac{D_{\text{CO}_2}^0}{\tau(z)} \quad (50)$$

Here $D_{\text{CO}_2}^0$ is used as the reference, all gases experience the same $D_{\text{eddy}}(z)$. The optimum α was $\alpha_{\text{EU}} = 0.27$ for the EU hole, and $\alpha_{\text{US}} = 0.35$ for the US hole.

3.3 Fit of modeled profiles to the data

The firn models were tuned separately to the US borehole, for which we have firn air data for four different tracers: CO_2 , CH_4 , SF_6 and $\delta^{15}\text{N}_2$. The fit to the data is shown in Fig. 5. As for the EU borehole we find a mismatch at depths $z > 70\text{m}$ for CO_2 (Fig. 5A); the feature is reproduced consistently by all the firn air models.

To assess how well the modeled profiles agree with the data we make a histogram of $(m_i - d_i)/\sigma_i$, where the index i goes over all the 77 data points of the US borehole. This is shown in Fig. 6 together with a Gaussian distribution of width $\sigma = 1$ and a surface area equal to that of the histogram.

The figure furthermore shows the root mean square deviation (RMSD) from the data as given by Eq. (3) of the main text. Most models perform better for the US borehole in terms of the RMSD, which is due to the fact that there are fewer tracers for the US borehole. This means the effective diffusivity profile is less strongly constrained, allowing for more degrees of freedom in the tuning procedure. The exception is the CSIRO model for which the RMSD is higher on the US hole. However, preliminary tests show that by including the advective backflux in the CSIRO model the RMSD improves to 0.79 (Trudinger et al., in preparation).

4 Model intercomparison

4.1 Diffusivity profiles and gas age distributions

Figure 7A shows the reconstructed molecular diffusivity profiles for CO_2 for the different models on the US borehole. Upon reaching the LIZ the effective molecular diffusion

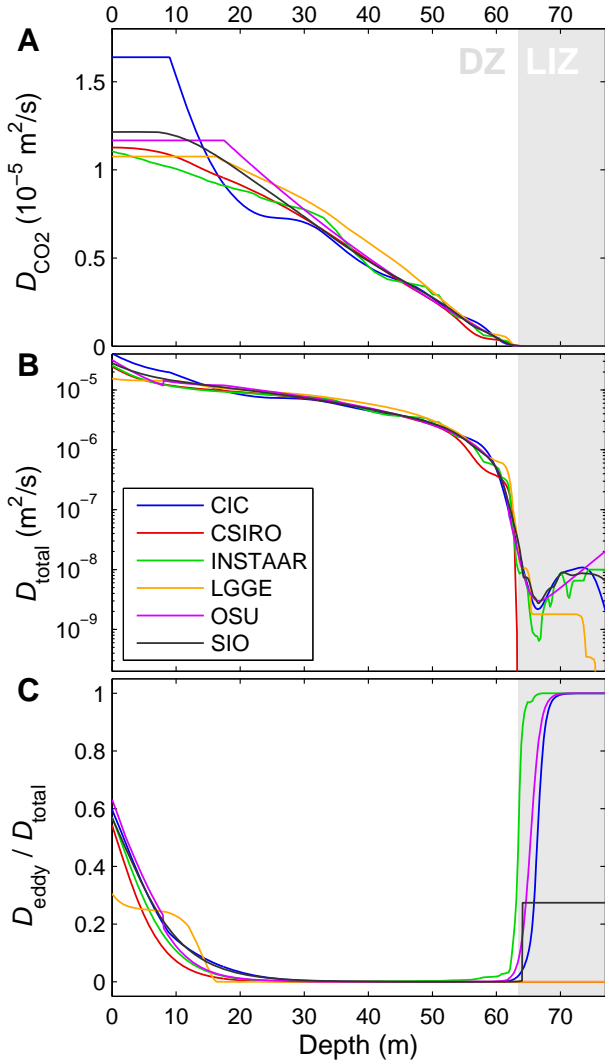


Fig. 7. (A) CO_2 molecular diffusivity profile with depth $D_{\text{CO}_2}(z)$ for the US borehole. (B) Semi-log plot of the total CO_2 diffusivity profile $D_{\text{total}}(z) = D_{\text{CO}_2}(z) + D_{\text{eddy}}$. (C) Plot of $D_{\text{eddy}}(z)/D_{\text{total}}(z)$. The eddy diffusion near the surface corresponds to the convective mixing, in the LIZ some of the models have included dispersive mixing.

nearly vanishes. In Fig. 7B the total diffusivity $D_{\text{total}}(z) = D_{\text{CO}_2}(z) + D_{\text{eddy}}$ for CO_2 is plotted on a semilog scale. As for the EU borehole we observe that the models require a non-vanishing diffusivity within the LIZ to fit the data. Only the CSIRO model uses zero diffusivity in the LIZ for the US hole. This difference might explain why the CSIRO model has more difficulty fitting the US data, as expressed by the RMSD in Fig. 6.

Figure 8 compares age distribution densities for the models at the lock-in depth ($z = 63$ m) and near the deepest sample ($z = 76$ m) on the US hole. Table 14 gives some characteristics of the distributions. On the EU hole we find a spread

Table 14. Mean age, median age, Full Width at Half Maximum and Spectral Width (Δ , Eq. (1) in Trudinger et al., 2002) at the lock-in depth ($z = 63$ m) and bottom of the LIZ ($z = 76$ m) for the US borehole. All values given in years.

Model	Mean	Median	FWHM	Δ
$z = 63$ m				
CIC	8.5	6.9	7.2	4.0
CSIRO	7.5	6.3	6.4	3.1
INSTAAR	7.9	6.4	6.6	3.7
LGGE-GIPSA	12.4	8.4	8.5	8.3
OSU	8.4	6.8	7.1	4.0
SIO	8.3	6.7	7.0	3.9
$z = 76$ m				
CIC	61.8	58.3	39.8	14.6
CSIRO	60.4	59.3	6.4	3.1
INSTAAR	63.7	60.7	39.8	14.0
LGGE-GIPSA	69.0	66.4	34.6	12.3
OSU	62.3	59.1	40.3	14.2
SIO	62.7	59.2	41.5	14.8

of up to 30% in the mean ages and distribution widths. When looking at the US hole the spread in the calculated mean ages is even larger (up to 50%). This large spread is mostly due to the LGGE-GIPSA model, which stands out as having a wider and flatter age distribution. However, since this model obtains a better fit to the experimental data than most models (Fig. 6) this distribution is certainly realistic. We attribute the larger spread found in modeled US borehole mean ages to the fact that it has fewer tracers. This leaves the mean age more poorly constrained. The CSIRO age distribution at $z = 76$ m is very narrow compared to the other models, due to the absence of LIZ diffusion in the US hole. Since it differs so strongly from both the CSIRO model result on the EU hole, as well as from the other model results on the US hole, this age distribution was not included in the comparison in Fig. 7 of the main article.

4.2 Synthetic diagnostic scenarios

Table 15 provides detailed specifications on how the diagnostic scenarios are run in the models.

Scenario I compares the amount of diffusive fractionation (DF) of isotopes in the firn. We model the mole fractions of $^{12}\text{CO}_2$ and $^{13}\text{CO}_2$ separately using the relative diffusion coefficients given in Sect. 3.1.2. For convenience we let our reference atmosphere have the property

$$^{13}R_{\text{std}} = \left. \frac{[^{13}\text{CO}_2]}{[^{12}\text{CO}_2]} \right|_{\text{std}} = 1 \quad (51)$$

meaning that at in the atmosphere $[^{12}\text{CO}_2] = [^{13}\text{CO}_2]$ as we let the mixing ratio increase with time. We use the same atmospheric input file to force both isotopologues. The fractionation with depth is then given as

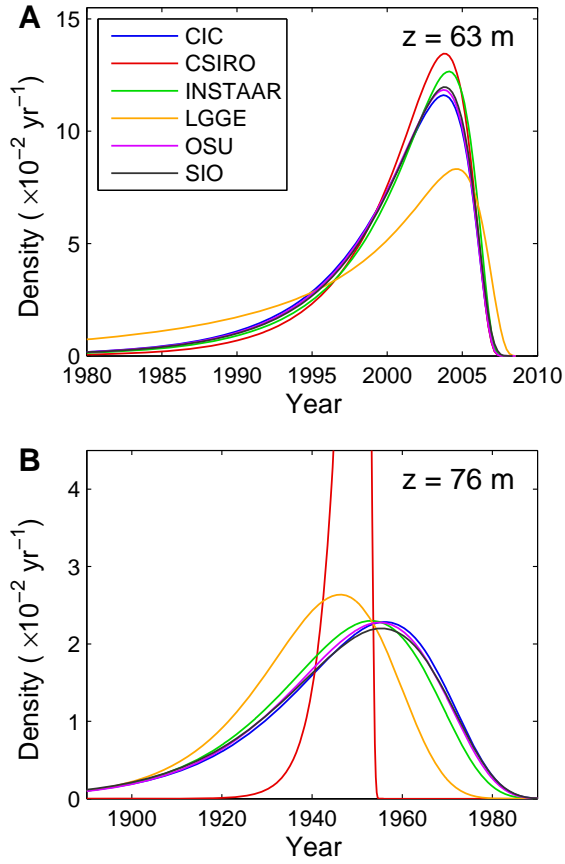


Fig. 8. US borehole modeled age distribution densities for (depth $z = 63\text{m}$ (lock-in depth)). On the horizontal axis are calendar years C.E.; decimal sampling year is 2008.54 (i.e. mid July). Age distributions are generated by applying a surface forcing which is unity for $0.2 \leq t < 0.4$ yr, and zero elsewhere.

$$\delta^{13}\text{CO}_2(z) = \left(\frac{[^{13}\text{CO}_2](z)}{[^{12}\text{CO}_2](z)} - 1 \right) \times 10^3 \quad (52)$$

Finally we look at the scenario comparison for models run with their effective diffusivity tuned to the US borehole, the outcome of which is shown in Fig. 9. We observe similar model differences as on the EU borehole. For scenario I (Fig. 9A) we see a large discrepancy in modeled diffusive isotopic fractionation between the firn models. The magnitude of the model discrepancy is similar to that of the EU borehole. For scenario II we see that the CSIRO model has no diffusion in the LIZ, contrary to the other models. This is related to the CSIRO reconstructed diffusivity profile, which goes to zero in the LIZ (Fig. 7B). Scenario IV is identical between the two boreholes, since the advective transport term depends only on the porosity parameterisation and accumulation rate which are the same for both boreholes.

Notation

A	Accumulation rate (myr^{-1} ice equivalent)
A_{abs}	Absolute ^{14}C abundance (1.1764×10^{-12})
C	Mixing ratio (molmol^{-1})
D_{eddy}	Eddy diffusion coefficient (m^2s^{-2})
D_X	Diffusion coefficient of gas X (m^2s^{-2})
D_X^0	Free air diffusion coeff. of gas X (m^2s^{-2})
d_i	Data point i
g	Gravitational acceleration (9.82 ms^{-2})
J	Trace gas flux ($\text{molmol}^{-1}\text{ms}^{-1}$)
M_{air}	Molar mass of air (kgmol^{-1})
M_X	Molar mass of gas X (kgmol^{-1})
m_i	Modeled value for data point i
p	Air pressure (Pa)
$p_{\text{H}_2\text{O}}$	Vapour pressure of water (Pa)
R	Molar gas constant ($8.314 \text{ Jmol}^{-1}\text{K}^{-1}$)
RMSD	Root Mean Square Deviation
s	Total porosity (m^3m^{-3})
s_{co}	Mean close-off porosity (m^3m^{-3})
$s_{\text{op}(\text{cl})}$	Open (closed) porosity (m^3m^{-3})
s_{op}^*	Effective open porosity (m^3m^{-3})
T	Absolute temperature (K)
u_X	Uncertainty in gas X (molmol^{-1})
V_{contam}/V	Fraction of contamination (m^3m^{-3})
w_{air}	Downward velocity of air (ms^{-1})
w_{ice}	Downward velocity of ice layers (ms^{-1})
$[X]$	Mixing ratio of gas X (molmol^{-1})
x_{air}	Air content of ice (mL STP per kg ice)
z	Depth (m)
z_{COD}	Full close-off depth; $s_{\text{op}}(z_{\text{COD}}) = 0$ (m)
z_{LID}	Lock-in depth (m)
γ_X	Diffusion coefficient relative to CO_2
Δage	Ice age-gas age difference (yr)
$\Delta\text{age}_{\text{op}}$	Ice age- open pore gas age difference (yr)
ΔM	Molar mass deviation from air (kgmol^{-1})
Δt	Temporal step size (s) or (yr)
Δz	Spatial step size (m)
δ_{grav}	Gravitational fractionation p. unit mass (‰)
Θ	Temperature ($^{\circ}\text{C}$)
θ	Trapping rate (s^{-1})
λ_X	Radioactive decay constant of gas X (s^{-1})
ρ	Firn density (gcm^{-3})
ρ_{co}	Mean close-off density (gcm^{-3})
ρ_{COD}	Full close-off density; $\rho(z_{\text{COD}})$ (gcm^{-3})
ρ_{ice}	Solid ice density (gcm^{-3})
σ_i	Assigned uncertainty for data point i
τ	Tortuosity
τ_0	Initial guess for τ in tuning algorithm
$\phi_{\text{op}(\text{cl})}$	Air flux in open (closed) porosity (ms^{-1})

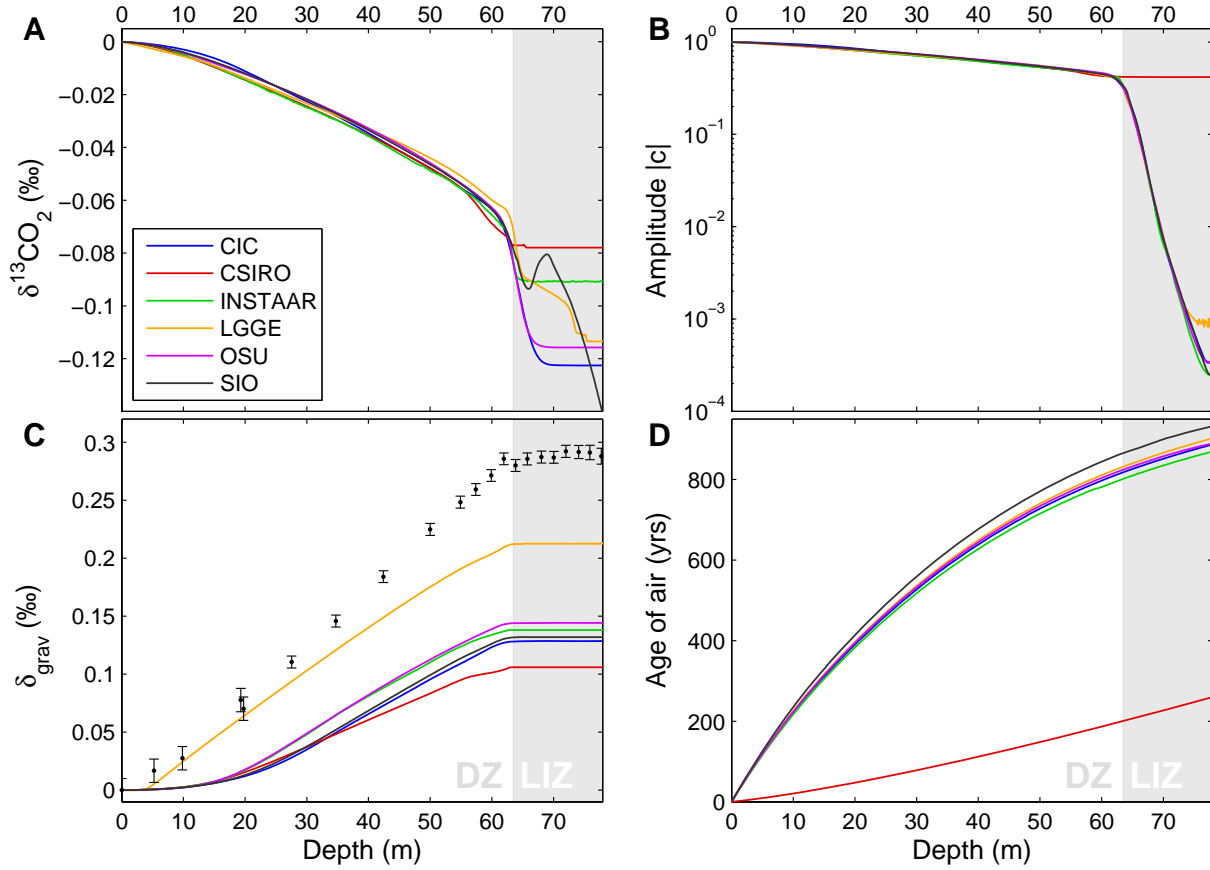


Fig. 9. Model comparison using the four diagnostic scenarios and diffusivity tuned to the US borehole data. (A) Scenario I: Diffusive fractionation for a hypothetical monotonic CO₂ increase. (B) Scenario II: Attenuation of a 15 yr period sinusoidal CO₂ forcing with depth. (C) Scenario III: Gravitational enrichment for gas X with $D_X^0 = 0.025D_{\text{CO}_2}^0$. Data points show gravitational enrichment of ¹⁵N₂ corrected for the effect of thermal diffusion. (D) Scenario IV: Mean age of gas Y, using advective transport only ($D_Y^0 = 0$). With the exception of S-III all scenarios were run with the effect of gravity turned off.

Table 15. Details on running the diagnostic scenarios.

Gas	Mass (g mol ⁻¹)	D/D_{CO_2}	Scenario file	Gravity	Run time (yr CE)
Scenario I					
¹² CO ₂	43.99	1.000048	Diagnostic_1.txt	OFF	1800-2008.54
¹³ CO ₂	44.99	0.995613	Diagnostic_1.txt	OFF	1800-2008.54
Scenario II					
CO ₂	44.01	1	Diagnostic_2a.txt	OFF	1800-2008.54
CO ₂	44.01	1	Diagnostic_2b.txt	OFF	1800-2008.54
Scenario III					
X	$M_{\text{air}}+1$	0.025	Diagnostic_3.txt	ON	1000-2008.54
Scenario IV					
Y	44.01	0	Diagnostic_4.txt	OFF	400-2008.54

References

- Arnaud, L., Barnola, J. M., and Duval, P.: Physical modeling of the densification of snow/firn and ice in the upper part of polar ice sheets, in: *Physics of Ice Core Records*, edited by Hondoh, T., pp. 285–305, Hokkaido University Press, 2000.
- Barr, R. F. and Watts, H.: Diffusion of some organic and inorganic compounds in air, *J. Chem. Eng. Data*, 17, 45–46, 1972.
- Blanc, A.: Recherches sur les mobilités des ions dans les gaz, *J. Phys. Theor. Appl.*, 7, 825–839, 1908.
- Bzowski, J., Kestin, J., Mason, E. A., and Uribe, F.: Equilibrium and transport properties of gas mixtures at low density: eleven polyatomic gases and five noble gases, *J. Phys. Chem. Ref. Data*, 19, 1179–1232, 1990.
- Chen, N. H. and Othmer, D. F.: New Generalized Equation for Gas Diffusion Coefficient, *J. Chem. Eng. Data*, 7, 37–41, 1962.
- Colbeck, S. C.: Air movement in snow due to windpumping, *J. Glaciol.*, 35, 209–213, 1989.
- Cowie, M. and Watts, H.: Diffusion of methane and chloromethanes in air, *Can. J. Chem.*, 49, 74–77, 1971.
- Craig, H.: Isotopic standards for carbon and oxygen and correction factors for mass-spectrometric analysis of carbon dioxide, *Geochim. Cosmochim. Ac.*, 12, 133–149, 1957.
- CRC: *CRC Handbook of Chemistry and Physics*, 83rd Edition, CRC Press, Boca Raton, FL, USA, 2002.
- Etheridge, D., Steele, L., Francey, R., and Langenfelds, R.: Atmospheric methane between 1000 AD and present: Evidence of anthropogenic emissions and climatic variability, *J. Geophys. Res.-Atm.*, 103, 15 979–15 993, 1998.
- Etheridge, D. M., Steele, L. P., Langenfelds, R. L., Francey, R. J., Barnola, J. M., and Morgan, V. I.: Natural and anthropogenic changes in atmospheric CO₂ over the last 1000 years from air in Antarctic ice and firn, *J. Geophys. Res.*, 101, 4115–4128, 1996.
- Fink, D., Hotchkis, M., Hua, Q., Jacobsen, G., Smith, A., Zoppi, U., Child, D., Mifsud, C., van der Gaast, H., Williams, A., and Williams, M.: The ANTARES AMS facility at ANSTO, *Nucl. Instrum. Meth. B*, 223, 109–115, 2004.
- Francey, R., Allison, C., Etheridge, D., Trudinger, C., Enting, I., Leuenberger, M., Langenfelds, R., Michel, E., and Steele, L.: A 1000-year high precision record of delta C-13 in atmospheric CO₂, *Tellus B*, 51, 170–193, 1999.
- Fuller, E. N., Schettler, P. D., and Giddings, J. C.: A new method for prediction of binary gas-phase diffusion coefficients, *Ind. Eng. Chem.*, 58, 19–27, 1966.
- Gilliland, E. R.: Diffusion coefficients in gaseous systems, *Ind. Engng. Chem.*, 26, 681–685, 1934.
- Goujon, C., Barnola, J. M., and Ritz, C.: Modeling the densification of polar firn including heat diffusion: Application to close-off characteristics and gas isotopic fractionation for Antarctica and Greenland sites, *J. Geophys. Res.-Atm.*, 108, 18, 2003.
- Guzman, M. I., Hoffmann, M. R., and Colussi, A. J.: Photolysis of pyruvic acid in ice: Possible relevance to CO and CO₂ ice core record anomalies, *J. Geophys. Res.-Atm.*, 112, 10, 2007.
- Haupt, R. L. and Haupt, S. E.: *Practical Genetic Algorithms*, John Wiley & Sons, Inc., Hoboken, New Jersey, 1998.
- Herron, M. M. and Langway, C. C.: Firn densification - an empirical model, *J. Glaciol.*, 25, 373–385, 1980.
- Hua, Q. and Barbetti, M.: Review of tropospheric bomb C-14 data for carbon cycle modeling and age calibration purposes, *Radiocarbon*, 46, 1273–1298, 2004.
- Huber, C., Beyerle, U., Leuenberger, M., Schwander, J., Kipfer, R., Spahni, R., Severinghaus, J. P., and Weiler, K.: Evidence for molecular size dependent gas fractionation in firn air derived from noble gases, oxygen, and nitrogen measurements, *Earth Planet Sc. Lett.*, 243, 61–73, 2006.
- Karlen, I., Olsson, I. U., Kallburg, P., and Kilici, S.: Absolute determination of the activity of two ¹⁴C dating standards, *Arkiv Geofysik*, 4, 465–471, 1968.
- Kawamura, K., Severinghaus, J. P., Ishidoya, S., Sugawara, S., Hashida, G., Motoyama, H., Fujii, Y., Aoki, S., and Nakazawa, T.: Convective mixing of air in firn at four polar sites, *Earth Planet Sc. Lett.*, 244, 672–682, 2006.
- Lal, D., Jull, A. J. T., Donahue, D. J., Burtner, D., and Nishiizumi, K.: Polar ice ablation rates measured using in-situ cosmogenic C-14, *Nature*, 346, 350–352, 1990.
- Levin, I. and Kromer, B.: The tropospheric (CO₂)-C-14 level in mid-latitudes of the Northern Hemisphere (1959-2003), *Radiocarbon*, 46, 1261–1272, 2004.
- Levin, I., Naegler, T., Heinz, R., Osusko, D., Cuevas, E., Engel, A., Ilmberger, J., Langenfelds, R. L., Neining, B., Rohden, C. v., Steele, L. P., Weller, R., Worthy, D. E., and Zimov, S. A.: The global SF₆ source inferred from long-term high precision atmospheric measurements and its comparison with emission inventories, *Atmos. Chem. Phys.*, 10, 2655–2662, 2010.
- Levin, I., Hammer, S., Kromer, B., and Meinhardt, F.: Radiocarbon observations in atmospheric CO₂: Determining fossil fuel CO₂ over Europe using Jungfraujoch observations as background, *Sci. Total Environ.*, 391, 211–216, 2008.
- Levin, I., Naegler, T., Kromer, B., Diehl, M., Francey, R. J., Gomez-Pelaez, A. J., Steele, L. P., Wagenbach, D., Weller, R., and Worthy, D. E.: Observations and modelling of the global distribution and long-term trend of atmospheric (CO₂)-C-14, *Tellus B*, 62, 207, 2010.
- Lugg, G. A.: Diffusion coefficients of some organic and other vapors in air, *Anal. Chem.*, 40, 1072–1077, 1968.
- Manning, M. and Melhuish, W. H.: *Atmospheric Delta 14C record from Wellington*, in: *Trends: A Compendium of Data on Global Change*, Carbon Dioxide Information Analysis Center, Oak Ridge National Laboratory, U.S. Department of Energy, Oak Ridge, Tenn., U.S.A., 1994.
- Marrero, T. R. and Mason, E. A.: Gaseous diffusion coefficients, *J. Phys. Chem. Ref. Data*, 1, 3–118, 1972.
- Martinerie, P., Raynaud, D., Etheridge, D. M., Barnola, J. M., and Mazaudier, D.: Physical and climatic parameters which influence the air content in polar ice, *Earth Planet Sc. Lett.*, 112, 1–13, 1992.
- Martinerie, P., Lipenkov, V. Y., Raynaud, D., Chappellaz, J., Barkov, N. I., and Lorius, C.: Air content paleo record in the Vostok ice core (Antarctica): A mixed record of climatic and glaciological parameters, *J. Geophys. Res.*, 99, 10 565–10 576, 1994.
- Martinerie, P., Nourtié-Mazaauric, E., Barnola, J. M., Sturges, W. T., Worton, D. R., Atlas, E., Gohar, L. K., Shine, K. P., and Brasseur, G. P.: Long-lived halocarbon trends and budgets from atmospheric chemistry modelling constrained with measurements in polar firn, *Atmos. Chem. Phys.*, 9, 3911–3934, 2009.
- Massman, W. J.: A review of the molecular diffusivities of H₂O, CO₂, CH₄, CO, O₃, SO₂, NH₃, N₂O, NO, and NO₂ in air, O₂ and N₂ near STP, *Atmos. Environ.*, 32, 1111–1127, 1998.

- Massman, W. J.: Molecular diffusivities of Hg vapor in air, O₂ and N₂ near STP and the kinematic viscosity and thermal diffusivity of air near STP, *Atmos. Environ.*, 33, 453–457, 1999.
- Matsunaga, N., Hori, M., and Nagashima, A.: Mutual diffusion coefficients of halogenated-hydrocarbon refrigerant-air systems, *High Temp.-High Press.*, 25, 185–192, 1993.
- Matsunaga, N., Hori, M., and Nagashima, A.: Diffusion coefficients of global warming gases into air and its component gases, *High Temp.-High Press.*, 30, 77–83, 1998.
- Matsunaga, N., Hori, M., and Nagashima, A.: Measurements of the mutual diffusion coefficients of gases by the Taylor method (7th Report, measurements on the SF₆-air, SF₆-N₂, SF₆-O₂, CFC12-N₂, CFC12-O₂, HCFC22-N₂ and HCFC22-O₂ systems), *Trans. Jpn. Soc. Mech. Eng. B.*, 68, 550–555, 2002a.
- Matsunaga, N., Hori, M., and Nagashima, A.: Measurements of mutual diffusion coefficients gases by the Taylor method: measurements on H₂-air, H₂-N₂, and H₂-O₂ systems, *Heat Trans. Asian Res.*, 31, 182–193, 2002b.
- Matsunaga, N., Hori, M., and Nagashima, A.: Measurements of the mutual diffusion coefficients of gases by the Taylor method (8th Report, measurements on the HFC32-air, HCFC124-air, HCFC125-air, HCFC143a-air, and HFC43-10mee-air systems), *Trans. Jpn. Soc. Mech. Eng. B.*, 68, 550–555, 2002c.
- Matsunaga, N., Hori, M., and Nagashima, A.: Measurements of the mutual diffusion coefficients of carbon tetrafluoride and methyl bromide into air, nitrogen and oxygen, *Proc 26th Jpn Symp Therm Props*, 26, 499–501, 2005.
- Matsunaga, N., Hori, M., and Nagashima, A.: Gaseous diffusion coefficients of dimethyl ether and diethyl ether into air, nitrogen and oxygen, *Netsu Bussei*, 20, 83–86, 2006.
- Matsunaga, N., Hori, M., and Nagashima, A.: Gaseous diffusion coefficients of propane and propylene into air, nitrogen and oxygen, *Netsu Bussei*, 20, 83–86, 2007.
- Matsunaga, N., Hori, M., and Nagashima, A.: Gaseous diffusion coefficients of methyl bromide and methyl iodide into air, nitrogen and oxygen, *Heat Trans. Asian Res.*, 38, doi:10.1002/htj.20255, 2009.
- Nydal, R. and Lövseth, K.: Carbon-14 Measurements in Atmospheric CO₂ from Northern and Southern Hemisphere Sites, 1962-1993, Carbon Dioxide Information Analysis Center, Oak Ridge National Laboratory, Oak Ridge, Tennessee, 1996.
- Reimer, P., Baillie, M., Bard, E., Bayliss, A., Beck, J., Bertrand, C., Blackwell, P., Buck, C., Burr, G., Cutler, K., Damon, P., Edwards, R., Fairbanks, R., Friedrich, M., Guilderson, T., Hogg, A., Hughen, K., Kromer, B., McCormac, G., Manning, S., Ramsey, C., Reimer, R., Remmele, S., Southon, J., Stuiver, M., Talamo, S., Taylor, F., van der Plicht, J., and Weyhenmeyer, C.: IntCal04 terrestrial radiocarbon age calibration, 0-26 cal kyr BP, *Radiocarbon*, 46, 1029–1058, 2004.
- Rommelaere, V., Arnaud, L., and Barnola, J. M.: Reconstructing recent atmospheric trace gas concentrations from polar firn and bubbly ice data by inverse methods, *J. Geophys. Res.-Atm*, 102, 30 069–30 083, 1997.
- Schwander, J.: The transformation of snow to ice and the occlusion of gases, in: *The Environmental record in glaciers and ice sheets*, edited by Oeschger, H. and Langway, C., pp. 53–67, John Wiley, New York, 1989.
- Schwander, J., Stauffer, B., and Sigg, A.: Air mixing in firn and the age of the air at pore close-off, in: *Ann. Glaciol.*, vol. 10, pp. 141–145, 1988.
- Schwander, J., Barnola, J. M., Andrie, C., Leuenberger, M., Ludin, A., Raynaud, D., and Stauffer, B.: The age of the air in the firn and the ice at Summit, Greenland, *J. Geophys. Res.-Atm*, 98, 2831–2838, 1993.
- Severinghaus, J. P. and Battle, M. O.: Fractionation of gases in polar lee during bubble close-off: New constraints from firn air Ne, Kr and Xe observations, *Earth Planet Sc. Lett.*, 244, 474–500, 2006.
- Severinghaus, J. P., Grachev, A., and Battle, M.: Thermal fractionation of air in polar firn by seasonal temperature gradients, *Geochem. Geophys. Geosy.*, 2, 2001.
- Severinghaus, J. P., Albert, M. R., Courville, Z. R., Fahnestock, M. A., Kawamura, K., Montzka, S. A., Muhle, J., Scambos, T. A., Shields, E., Shuman, C. A., Suwa, M., Tans, P., and Weiss, R. F.: Deep air convection in the firn at a zero-accumulation site, central Antarctica, *Earth Planet Sc. Lett.*, 293, 359–367, 2010.
- Sowers, T., Bender, M., Raynaud, D., and Korotkevich, Y. S.: Delta-N-15 of N₂ in air trapped in polar ice - a tracer of gas-transport in the firn and a possible constraint on ice age-gas age-differences, *J. Geophys. Res.-Atm*, 97, 15 683–15 697, 1992.
- Stuiver, M. and Polach, H. A.: Reporting of C-14 data - discussion, *Radiocarbon*, 19, 355–363, 1977.
- Trudinger, C. M., Enting, I. G., Etheridge, D. M., Francey, R. J., Levchenko, V. A., Steele, L. P., Raynaud, D., and Arnaud, L.: Modeling air movement and bubble trapping in firn, *J. Geophys. Res.-Atm*, 102, 6747–6763, 1997.
- Trudinger, C. M., Etheridge, D. M., Rayner, P. J., Enting, I. G., Sturrock, G. A., and Langenfelds, R. L.: Reconstructing atmospheric histories from measurements of air composition in firn, *J. Geophys. Res.-Atm*, 107, 13, 2002.
- Tschumi, J. and Stauffer, B.: Reconstructing past atmospheric CO₂ concentration based on ice-core analyses: open questions due to in situ production of CO₂ in the ice, *J. Glaciol.*, 46, 45–53, 2000.
- Watts, H.: Temperature dependence of the diffusion of carbon tetrachloride, chloroform, and methylene chloride vapors in air by a rate of evaporation method, *Can. J. Chem.*, 49, 67–73, 1971.
- Witrant, E. and Martinerie, P.: A Variational Approach for Optimal Diffusivity Identification in Firns, in: *Proc. of the 18th Med. Conf. on Control and Automation*, pp. 892–897, Marrakech, Morocco, 2010.
- WMO: Scientific Assessment of Ozone Depletion: 2006. Global Ozone Research and Monitoring Project - Report No.50, World Meteorological Organization, Geneva, <http://ozone.unep.org/Publications>, 2007.
- Yoshida, N. and Toyoda, S.: Constraining the atmospheric N₂O budget from intramolecular site preference in N₂O isotopomers, *Nature*, 405, 330–334, 2000.